THESIS

SEASONAL TO MULTI-DECADAL VARIABILITY OF THE WIDTH OF THE

TROPICAL BELT

Submitted by

Nicholas Alexander Davis

Department of Atmospheric Science

In partial fulfillment of the requirements

For the Degree of Master of Science

Colorado State University

Fort Collins, Colorado

Summer 2013

Master's Committee:

    Advisor: Thomas Birner

    David Thompson
    Karan Venayagamoorthy

ABSTRACT

SEASONAL TO MULTI-DECADAL VARIABILITY OF THE WIDTH OF THE
TROPICAL BELT

An expansion of the tropical belt has been extensively reported in observations,
reanalyses, and climate model simulations, but there is a great deal of uncertainty in
estimates of the rate of widening as different diagnostics give a wide range of results. This
study critically examines robust diagnostics for the width of the tropical belt to explore
their seasonality, interannual variability, and multi-decadal trends. These diagnostics are
motivated by an exploration of two simple models of the Hadley circulation and subtropical
jets.

The width based on the latitudes of the maximum tropospheric dry bulk static stability,
measuring the difference in potential temperature between the tropopause and the surface,
is found to be closely coupled to the width based on the subtropical jet cores on all
timescales. In contrast, the tropical belt width and Northern Hemisphere edge latitudes
based on the latitudes at which the vertically-averaged streamfunction vanishes, a measure
of the Hadley circulation's poleward edges, lags those of the other diagnostics by
approximately one month. The tropical belt width varies by up to ten degrees latitude
among the diagnostics, with trends in the tropical belt width ranging from -0.5 to 2.0
degrees per decade over the 1979-2012 period. Nevertheless, in agreement with previous
studies nearly all diagnostics exhibit a widening trend, although the streamfunction
diagnostic exhibits a significantly stronger widening than either the jet or dry bulk stability

diagnostics. Finally, GPS radio occultation observations are used to assess the ability of the reanalyses to reproduce the tropical belt width, finding that they better situate the latitudes of maximum bulk stability versus those of the subtropical jets.

ACKNOWLEDGEMENTS

TABLE OF CONTENTS

1 Introduction

Understanding the width of the Hadley cell is important from a purely scientific perspective, as it is a basic parameter of the general circulation that delineates the boundary between the tropical and extratropical circulations. The subtropics straddle this boundary, dried by both the convergence of moisture into the rising branch and adiabatic compression in the subsiding branches of the Hadley cells.

Quantifying past and future changes in this region is crucial in estimating the earth's climate sensitivity and projecting future impacts from anthropogenic climate change. For example, the marine stratocumulus decks in the subsiding branches of the Hadley and Walker circulations are where there is the greatest disagreement on the change in cloud radiative forcing both within model simulations of global warming and between models and reanalyses during the observational period (*Bony and Dufresne*, 2005). Further, there are significant human (*Kundzewicz et al.*, 2007) and ecological (*Fischlin et al.*, 2007) impacts associated with the projected drying and changes in the patterns of precipitation in the subtropics (*Meehl et al.*, 2007), although the changes specifically associated with a widening of the Hadley circulation are not entirely clear (*Seidel et al.*, 2009).

1.1 Uncertain trends in the tropical belt width

Climate simulations run for the Intergovernmental Panel on Climate Change: Assessment Report 4 project an expansion of the tropical belt and poleward shift of the subtropical dry zones as a response to increased greenhouse gas concentrations (*Lu et al. (1)*, 2007) while aquaplanet models have been shown to display tropical expansion

concurrent with an increase in global mean temperature (*Frierson et al.*, 2007). This consistency spanning model complexity suggests that the expansion of the Hadley circulation is a robust response to increased greenhouse gas concentrations, although the magnitude of the observed and expected widening continues to exhibit a large spread in the most advanced general circulation model runs in both the Coupled Model Intercomparison Project 3 (*Johanson and Fu*, 2009) and 5 (*Ceppi and Hartmann*, 2012).

Unfortunately, there remains significant uncertainty in how much the tropical belt has actually widened over the past three decades as different diagnostics and reanalyses used to evaluate the tropical belt edge latitudes display different trends (*Davis and Rosenlof*, 2012), with estimates ranging from tenths of a degree per decade based upon the jet streams (*Archer and Caldeira*, 2008) to degrees per decade based on ozone measurements of the subtropical and polar fronts (*Hudson*, 2012). Many of these diagnostics share a degree of subjectivity, being either threshold-based such as a specific tropopause height threshold (*Seidel and Randel*, 2007), or evaluated at a somewhat arbitrary vertical level such as the location where the 500 hPa streamfunction vanishes (*Hu and Fu* (2007); *Davis and Rosenlof* (2012); *Ceppi and Hartmann* (2012)). Trends assessed from these diagnostics could have been confounded by changes in the mean state of the atmosphere, for example the observed increase in the tropical tropopause height and deepening of the troposphere driven by recent tropospheric warming and stratospheric cooling (*Santer et al.*, 2003), and the choice of the subjective threshold can exert a strong influence on the magnitude of the derived trend (*Birner*, 2010). Ideally, the diagnostics used to estimate the tropical belt edge latitudes should be wholly objective, adaptable to changes in the mean state such as a vertical shift in the major features of the general circulation due to anthropogenic climate

forcings (*Singh and O'Gorman*, 2012) and solely measuring a feature of the general circulation that can be studied from simple equilibrium scaling arguments up to general circulation models.

However, rather than simply assessing decadal trends, we will examine the relationships between the diagnostics on seasonal and interannual timescales, hopefully shedding light on why the trends differ so substantially. It is evident from Figure 1 that the edge of the Hadley cell (the zero-contour of the mean meridional streamfunction) and the core of the subtropical jet and its associated subtropical tropopause break coincide in the subtropics. The subtropical jet emerges from the poleward flow in the Hadley circulation in simple scaling theories for the width of the Hadley circulation, e.g. *Held and Hou* (1980), while the tropopause break and subtropical jet core are both manifestations of the high baroclinicity in the subtropics. This study will examine these three features of the general circulation in detail, constructing objective diagnostics for the tropical belt edge latitudes that reflect both theory and observation.

1.2 Observational data

Further, while reanalyses are commonly used to study the tropical belt width, their use in trend analysis even when restricted to the satellite era should still be cautioned given the ever-changing nature of assimilated data from fewer in-situ to predominantly satellite-based observations (*Bengtsson et al.*, 2004), especially when examining trends in the tropics (*Trenberth and Fiorino*, 2001). As such, this study will also evaluate the ability

of the reanalyses to reproduce the seasonal cycle and interannual variability of the width of the tropical belt as estimated from observational data.
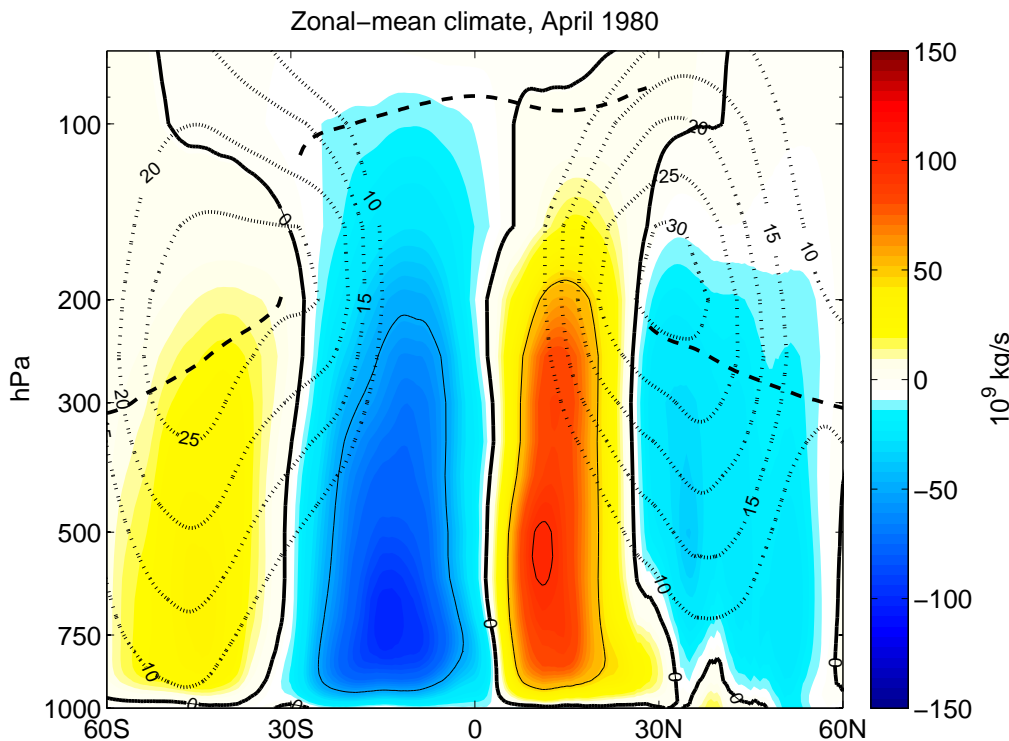
Figure 1: The zonal-mean circulation and atmospheric structure for April 1980, derived from MERRA. Shading indicates the mean meridional streamfunction (defined later in the text) in 10^9 kg/s, dotted contours indicate the zonal-mean zonal wind in m/s, and the thick, dashed line indicates the tropopause pressure.

However, the mean meridional circulation cannot be resolved using the upper-air network due to a lack of wind observations over the oceans (*Waliser et al.*, 1999), which presumably presents problems in reconstructing the jet streams, too. While there are various satellite products offering vertical profiles of temperature, the accuracy and precision required for this study presents a unique opportunity for using global positioning system radio occultation (GPS-RO) data, which has global coverage at fine vertical resolution over the past decade. Herein we introduce a new simple and objective temperature-based diagnostic that can be directly assessed with GPS-RO data and use

4

both temperature and pressure profiles to study the subtropical jets via the geostrophic wind approximation.

1.3 The zonal mean

We will focus exclusively on the zonal mean circulation to explore the relationships between the diagnostics in as simple a context as possible, leaving a study of the longitudinal structure of these tropical belt width diagnostics to future work. As the Hadley cell is by definition a zonal mean construct, tropical belt widths and tropopause characteristics are derived from zonal-mean variables, as well, for consistency.

1.4 Outline

To begin, we describe the reanalysis products and GPS-RO data used in this thesis, and the technique used to grid the GPS-RO data, in Chapter 2. We then explore scaling theories and a new, modified model of the Hadley circulation and tropical belt in Chapter 3, and use the models to motivate a selection of the objective tropical belt diagnostics used herein to study the tropical belt width and edge latitudes.

In Chapter 4 we describe the details of our tropical belt width diagnostics and their calculations. In Chapter 5 we examine the seasonal cycles and variability of the three objective diagnostics, characterize the seasonal lag between the Hadley cell and subtropical jet, assess the long-term trends in the width of the tropical belt, and evaluate how the tropical belt width diagnostics are being reproduced by the reanalyses.

2 Data

Descriptions of GPS-RO and reanalysis products and a brief overview of the GPS-RO retrieval method are detailed in this section.

2.1 Global Positioning System radio occultation (GPS-RO)

2.1.1 COSMIC

GPS-RO data from the Constellation Observing System for Meteorology, Ionosphere, and Climate (COSMIC) (*Anthes et al.*, 2008) is sourced from the University Corporation for Atmospheric Research, providing around 2,000 vertical profiles of temperature and pressure on geometric altitude per day. GPS receivers on low earth orbit satellites receive L1 and L2 Doppler signals transmitted from GPS satellites that are refracted as they pass through the atmosphere. The resulting vertical profile of the bending angle of the signal can be used to recover the vertical profile of the refractive index at the occultation point using the Abel inversion (*Fjeldbo and Eshelman*, 1971). From *Anthes et al.* (2008), the refractive index, N, is shown to be a function of the temperature (T in Kelvin), of the atmospheric pressure (p in hectopascals), of the water vapor partial pressure (e in hectopascals), of the electron number density (n_e, number of electrons per cubic meter), and of the signal frequency (f in Hertz):

$$N = 77.6 \left(\frac{p}{T}\right) + \left(3.73 \times 10^5\right) \left(\frac{e}{T^2}\right) - \left(4.03 \times 10^7\right) \left(\frac{n_e}{f}\right) \tag{1}$$

In the neutral atmosphere the refractive index is solely a function of the dry air and water vapor densities, with the contribution from water vapor negligible at temperatures colder than 250 K (*Kursinski et al.*, 1996), or approximately above the 500 (400) mb level in the midlatitudes (tropics). In these regions the density profile can be calculated directly using the hydrostatic equation layer by layer to produce a profile of temperature and pressure. European Centre for Medium-Range Weather Forecasts (ECMWF) weather analyses are used as a first-guess temperature profile in an iterative method to first separate the density into its dry air and water vapor components before calculating profiles of temperature and pressure. Temperature accuracy in the tropical lower troposphere is on the order of 2 K, whereas it is ≈0.2 K in the lower stratosphere (*Kursinski et al.*, 1997). As noted in *Kursinski et al.* (2000), the GPS-RO technique suffers from a low horizontal resolution of up to ±200 km along the ray path at the tangent point.

2.1.2   CHAMP

GPS-RO data from the CHAllenging Satellite Mini Payload (CHAMP) (*Wickert et al.*, 2001) is also employed in this study, which provides on the order of 200 vertical profiles of temperature and pressure per day, an order of magnitude fewer than COSMIC. The retrieval process and post-processing is essentially identical to that of COSMIC.

2.1.3   Gridding technique

Daily COSMIC (CHAMP) profiles of temperature and pressure on geometric altitude are gridded onto a global three-dimensional grid at 2 (5) degree horizontal and 200 meter vertical resolution, respectively. For each day, GPS-RO profiles are gridded in a Cartesian

coordinate system with the origin at the center of the earth, rather than a latitude-longitude coordinate system, to ensure a proper weighting of distances between lines of longitude. However, given the high density of GPS-RO profiles, gridding in latitude-longitude space has no discernible effect on the final zonal-mean gridded product. To form monthly-mean fields, profiles are subdivided and gridded in 5- and 6-day bins within each month and then averaged, similar to the approach of *Leroy et al.* (2012). We construct a Delaunay triangulation of the irregularly-spaced GPS-RO profiles and then interpolate them to the grid using natural neighbor interpolation. The lowest-altitude temperature and pressure measurements from each profile are used to construct a seperate surface temperature and pressure field.

2.2 Reanalyses

Reanalysis products used in this study include the ECWMF Interim Reanalysis (*Dee et al.*, 2011), hereafter ERA-i, supplied by the ECMWF, the Modern-Era Retrospective Analysis (*Rienecker et al.*, 2011), hereafter MERRA, supplied by the National Aeronautics and Space Administration's Global Modeling and Assimilation Office, and the NCEP/NCAR Reanalysis (*Kalnay et al.*, 1996), hereafter NCEP, supplied by the National Oceanic and Atmospheric Administration's Earth System Research Laboratory's Physical Sciences Division. Reanalysis characteristics are summarized in Table 1. Despite different vertical resolutions, all of the reanalyses provide the same vertical resolution about the tropical tropopause, providing gridded data on the 150 hPa, 100 hPa, and 70 hPa pressure levels. In the tropical upper-troposphere this represents a vertical resolution of just under 1

km, much coarser than that offered by GPS-RO. It is worth mentioning that ERA-i has assimilated CHAMP, GRACE, and COSMIC radio occultations from 2001 onward and uses a 4D-var assimilation scheme (*Dee et al.*, 2011), whereas NCEP and MERRA do not employ GPS-RO observations and instead use a 3D-var assimilation scheme (*Rienecker et al.* (2011); *Kalnay et al.* (1996)).

Table 1: The total available data period, horizontal resolution, and number of standard pressure levels for each of the three reanalyses used.

Reanalysis	Data period	Resolution [° lat × ° lon]	Vertical levels
MERRA	1979-2012	$1/2° \times 2/3°$	42
ERA-i	1979-2012	$3/4° \times 3/4°$	37
NCEP	1948-2012	$2.5° \times 2.5°$	17

Our analysis spans the 1979-2011 period when all re-analyses have coverage, except when direct comparisons are made with COSMIC observations. In that case our analysis spans 2007-2011 when COSMIC has observations for each full calendar year.

3 Theoretical basis

The principal dynamical features invoked in studying the width of the tropical belt are the poleward termini of the Hadley cells and the latitudes of the subtropical jets, both closely connected in nearly-inviscid (*Held and Hou*, 1980), angular-momentum (AM)-conserving (*Held*, 2000), and quasi-AM-conserving scaling theories for the width of the Hadley circulation accounting for differences in the Rossby number between the winter and summer cells (*Kang and Lu*, 2012).

These scaling theories model the zonal flow in the Hadley cell's poleward-flowing upper branch as AM-conserving and neglect the effect of eddy momentum fluxes. Neglecting vertical advection, the zonal momentum equation is

$$\partial_t \overline{u} = (f + \overline{\zeta})\overline{v} - S = 0 \tag{2}$$

where f is the planetary vorticity, $\overline{\zeta}$ is the zonal-mean relative vorticity, S the eddy stress, $\overline{v}$ the zonal-mean meridional wind, and $\overline{u}$ the zonal-mean zonal wind. Before neglecting eddy stresses, we can already see that close to the equator where the Rossby number is close to unity (f is on the same order as $\overline{\zeta}$), the Coriolis torque is not in perfect balance with the eddy stress. That is, when $S = 0$, $\overline{v}$ is not necessarily zero. Neglecting the eddy stress, and seeking a nontrivial solution for the overturning circulation, we thus have

$$f + \overline{\zeta} = 0 \tag{3}$$

or in other words, conservation of angular momentum.

In the real atmosphere, eddies flux momentum out of the subtropical jet and the Hadley cell, broadening the cell to its observed width and strengthening the overturning in the summer cell (*Kim and Lee*, 2001). There is no current scaling theory of the Hadley circulation that unites the effect of the eddies, or macroturbulent circulations that drive the thermally-indirect Ferrel cell, with the thermally-direct Hadley cell. This is primarily due to the non-linear feedbacks between the two; wave-breaking latitudes and hence the distribution of the momentum fluxes depend upon the strength and structure of the background zonal flow, which itself is influenced by the eddies (*Andrews et al.*, 1987).

3.1   The nearly-inviscid limit

In the nearly-inviscid axisymmetric model examined in detail in *Held and Hou* (1980), the primary constraint on the circulation is Hide's theorem: there can be no extremum of angular momentum in the free atmosphere, except at the surface. Down-gradient diffusion of angular momentum due to a vanishingly-small (but still non-zero) viscosity cannot be balanced in the steady-state by advective fluxes of angular momentum because in the steady-state, the mass flux across any closed contour in the atmosphere must vanish. Thus, angular momentum must have its maximum at the equator and in a region of easterlies in the steady-state. Westerlies at the equator in the region of maximum angular momentum would produce a state of angular momentum greater than the maximum angular momentum of the earth's surface - so-called superrotation - that could only be supplied by up-gradient eddy fluxes of angular momentum. This creates a "boundary condition"

wherein everywhere in the atmosphere, the angular momentum must be less than or equal to that attained at the equator with a zonal velocity less than or equal to zero.

Consider the definition of angular momentum on the rotating sphere,

$$M = (\Omega a \cos \phi + u)a \cos \phi \tag{4}$$

where a is the mean radius of the Earth and ϕ is latitude. By Hide's theorem, the maximum angular momentum is attained at the equator and is $M = (\Omega a \cos 0°)a \cos 0° = \Omega a^2$. For Hide's theorem to be satisfied, the zonal wind u must thus satisfy the relationship $u \leq \Omega a(1/\cos \phi - \cos \phi)$, or equivalently, $u \leq \Omega a \sin^2(\phi)/\cos(\phi)$. We need to ask whether the radiative equilibrium geopotential height (temperature) field satisfies this condition.

On the monthly timescales that will be studied herein, the zonal wind can be assumed to be geostrophically-balanced,

$$fu + \frac{\tan(\phi)}{a}u^2 = -\frac{1}{a}\partial_\phi \Phi \tag{5}$$

where $\Phi = gz$ is the geopotential.

Using $u \leq \Omega a \sin^2(\phi)/\cos(\phi)$, and making the small-angle approximation (where $\sin(\phi) \approx \phi$ and $\cos(\phi) \approx 1 - \phi^2/2$ for small ϕ), we find that

$$2\Omega^2 a^2 \phi^3 \gtrsim -\partial_\phi \Phi \tag{6}$$

which states that the geopotential height can decrease at most as ϕ^4 in order to satisfy

12

Hide's theorem. As the geopotential height of a certain pressure level p can be described by the vertically-averaged temperature (via the hydrostatic approximation) $< T >$ of the column, the radiative-equilibrium temperature can also, at most, decrease as ϕ^4 with latitude in the tropics.

In the annual-mean, earth's vertically-averaged tropospheric radiative equilibrium temperature profile decreases with latitude approximately as

$$< T_E > \propto -\Delta_H \sin^2(\phi) \approx -\Delta_H \phi^2 \tag{7}$$

where Δ_H is the change in temperature from the equator to pole and $< T_E >$ is the radiative-equilibrium temperature (*Held and Hou*, 1980). Clearly, the radiatiave equilibrium temperature and thus geopotential height decrease faster than ϕ^4 in the tropics, thus there must exist a meridional circulation that draws the flow away from radiative equilibrium in order to satisfy Hide's theorem.

The geopotential height of the radiative equilibrium profile is

$$\Phi_E = -R < T_E > \ln\left(\frac{p}{p_0}\right) \tag{8}$$

where Φ_E is the radiative equilibrium geopotential height. The meridional gradient of the radiative equilibrium geopotential height field in (6) is given by

$$\partial_\phi \Phi_E = -R\partial_\phi < T_E > \ln\left(\frac{p}{p_0}\right) \approx 2R\phi\Delta_H \ln\left(\frac{p}{p_0}\right) \tag{9}$$

where we have used (7) to approximate the meridional derivative of $< T_E >$.

Combining (9) and (6),

$$2R\phi\Delta_H \ln\left(\frac{p}{p_0}\right) \approx 2\Omega^2 a^2 \phi^3 \tag{10}$$

$$\phi(z^*) \approx \left(\frac{gz^*}{\Omega^2 a^2}\frac{\Delta_H}{T_0}\right)^{(0.5)} \tag{11}$$

where $z^* = (-(RT_0)/g)\ln(p/p_0)$ is the log-pressure height and T_0 a reference temperature for the tropical atmosphere. While we have derived an analytical solution for the edge of the Hadley cell, *Held and Hou* (1980) were unable to create a steady-state, axisymmetric circulation in the nearly-inviscid limit, and further, the resulting circulations are baroclinically unstable and an order of magnitude too weak (*Schneider*, 2006).

Nevertheless, we can derive the Hadley cell extent and subtropical jet speed from the nearly-inviscid scaling relationship. Letting $\Omega = 7.292 \times 10^{-5}$ s^{-1}, $g = 9.8$ m/s, $a = 6.371 \times 10^6$ m, $T_0 = 295$ K and $\Delta_H = 60$ K representing a typical tropical reference temperature and equator-to-pole temperature contrast, respectively, $p_0 = 1000$ hPa, and $p = 100$ hPa a typical tropical tropopause pressure, we find a Hadley cell and subtropical jet extent of 25 degrees latitude. As will be shown later, this is narrower than the observed Hadley cell and subtropical jet extent, though it is reasonably close to the equinoctal extent.

Figure 2a shows the geopotential height of the tropical tropopause from the nearly-inviscid model for both the case of radiative equilibrium and the AM-conserving wind, reproducing Figure 1 from *Held and Hou* (1980). The intersection of the two profiles at 25 degrees latitude indicates the edge of the Hadley circulation. The difference between the AM-conserving and radiative equilibrium tropopause heights integrated from the

equator to the edge of the Hadley cell is zero; in other words, the Hadley circulation in this model is energetically-closed (*Schneider*, 2006).
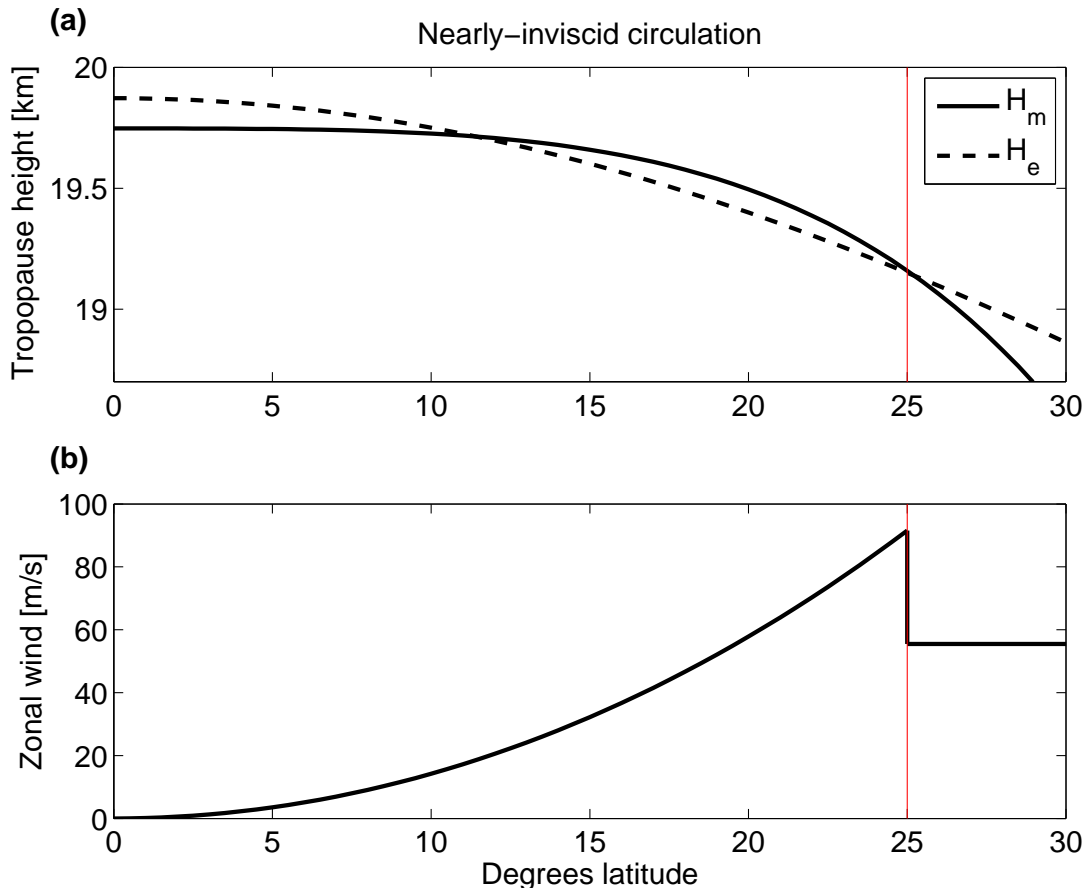
Figure 2: (a) Radiative equilibrium (H_e) and AM-conserving (H_m) geopotential height fields at 100mb, taken to be the tropical tropopause height, and (b) the resulting zonal wind profile using the nearly-inviscid axisymmetric model of *Held and Hou* (1980). The vertical red line is the analytical edge of the Hadley cell from the text. These figures are reproduced versions of Figure 1 and Figure 3 from *Held and Hou* (1980)

The nearly-inviscid model clearly predicts the existence of the subtropical jet, with zonal wind speeds peaking in the model profile in Figure 2b at the edge of the Hadley cell. Equatorward of the edge of the Hadley cell, the zonal wind conserves angular momentum as it moves poleward from the equator, rapidly increasing to 91 m/s. Outside of the Hadley cell, the zonal wind is in geostrophic balance with the radiative equilibrium height field,

and is approximately constant in the midlatitudes. The sharp discontinuity at 25 degrees latitude is unstable and exists as a subtropical jet core within two degrees latitude of that predicted by the scaling theory in numerical integrations (*Held and Hou*, 1980). The model correctly predicts a sharp gradient in the height of the tropopause in the subtropics and a nearly constant tropopause height in the deep tropics.

However, the log-pressure height of $z^* = 19$ km is significantly higher than the actual log-pressure or geometric height of the tropical tropopause, which typically range between 15.5 to 16.5 km, and the resulting subtropical jet speed at 25 degrees latitude is 91 m/s - about twice as large as the observed subtropical jet speed (see Figure 1). Clearly, angular momentum is not perfectly conserved in the Hadley cell, though the Rossby number is close to unity in the winter solsticial cell (*Schneider* (2006); *Kang and Lu* (2012)).

Lindzen and Hou (1988) studied the same nearly-inviscid model but instead allowed the latitude of maximum rising motion between the winter and summer cells to vary. They found that the strength and extent of the resulting circulation was nonlinearly-related to the latitude of rising motion, though this contrasts with observations of the seasonal cycle of the strength of the Hadley circulation (*Dima and Wallace*, 2003). Given the sum of the problems associated with nearly-inviscid axisymmetric theory, we cannot use the resulting scaling theory to speculate on possible changes to the extent of the Hadley circulation nor on the relationship between the jet and the Hadley cell.

3.2 Baroclinic instability

However, there is a simpler approach to studying the extent of the Hadley circulation and its relationship with the jet. Instead of prescribing a radiative equilibrium profile and demanding that the resulting circulation be energetically closed (*Schneider*, 2006), we can impose a more basic criterion: the poleward flow in the Hadley cell extends poleward until the resulting vertical shear is baroclinically unstable (*Held*, 2000). This solves the issue of baroclinically-unstable flow in the nearly-inviscid model (*Schneider*, 2006), eliminates the need to prescribe a radiative equilibrium profile, and also, albeit crudely, incorporates the effect of the eddies.

Following *Held* (2000), begin with the two-layer model's criterion for baroclinic instability,

$$\beta - \frac{f}{H_T}\partial_y H = 0 \tag{12}$$

where $\beta = \partial_y f$, H is the thickness of the upper layer, and H_T the height of the model lid, taken to be the height of the tropical tropopause. As the zonal flow in the lower layer is considered negligible, thermal wind balance becomes

$$g^*\partial_y H = f(u_1 - u_2) = f u_1 \tag{13}$$

where u_1 and u_2 are the zonal winds in the upper and lower layers and $g^* = g\Delta_v$ is the reduced gravity, with Δ_v the fractional change in potential temperature between the model

lid and the surface, $\Delta_v = 2(\theta_{trop} - \theta_{surf})/(\theta_{trop} + \theta_{surf})$. Combining (13) with (12), we find

$$u_1 = \beta \frac{g^* H_T}{f^2} \approx \frac{2\Omega(1 - \phi^2/2)}{a} \frac{g^* H_T}{4\Omega^2 \phi^2} \approx \frac{g^* H_T}{2\Omega a \phi^2} \qquad (14)$$

where we have again made the small-angle approximation.

Combining this with the requirement to satisfy Hide's theorem, $u \leq \Omega a \sin^2(\phi)/cos(\phi) \approx \Omega a \phi^2$, we find that the latitude at which the zonal flow in the upper branch of the Hadley cell becomes unstable is

$$\phi = \left(\frac{g \Delta_v H_T}{2\Omega^2 a^2} \right)^{0.25} \qquad (15)$$

(15) shows that the Hadley cell extent scales proportionally to the fractional change in potential temperature (the dry bulk static stability) and the tropopause height in the tropics. Given the observed (*Santer et al.*, 2003) and projected increases in tropopause height as a response to anthropogenic climate forcings (*Lorenz and DeWeaver*, 2007), the effect of a deepening troposphere is to increase the Hadley cell extent, as shown in Figure 3. Enhanced upper-tropospheric warming due to the lapse rate feedback associated with greenhouse gas forcings in general circulation models has been shown to increase dry stability throughout the troposphere (*Frierson*, 2006). Increasing dry stability effectively stabilizes the subtropical jet against baroclinic instability, allowing the Hadley cell to extend further poleward, also shown in Figure 3. The Hadley cell extent is equally-sensitive to equally-proportional changes in the tropopause height and fractional dry stability, expanding about 1 degree latitude for a $\approx 10\%$ increase in either.
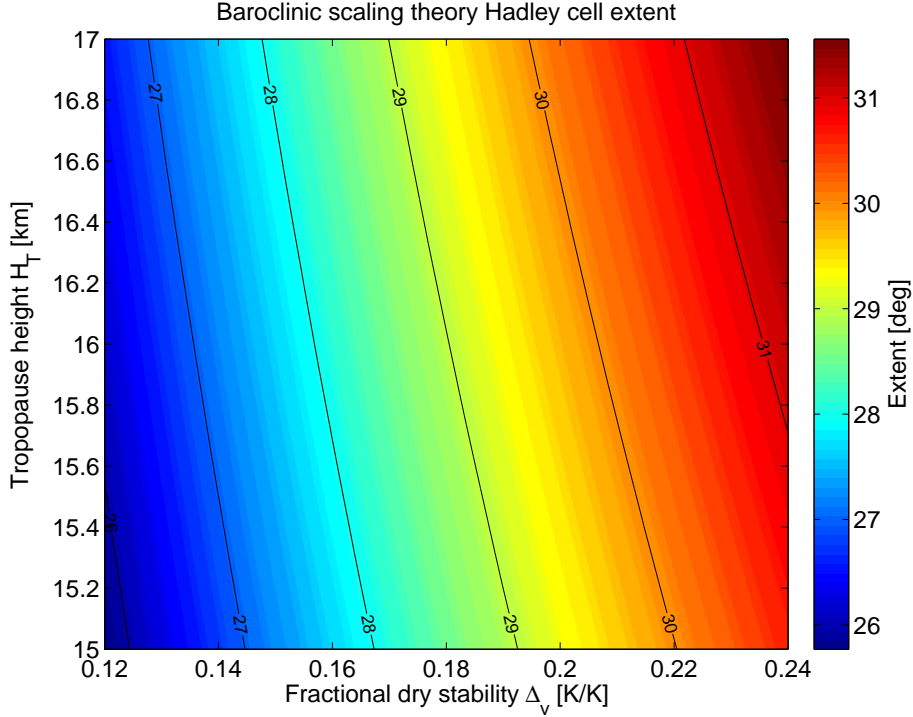
Figure 3: Hadley cell extent from the baroclinic scaling theory from *Held* (2000) for varying values of the fractional dry stability and tropopause height.

3.3 Seasonality and variability in an equilibrium model

The scaling theory can be modified to allow the latitude of rising motion separating the Northern and Southern Hemisphere Hadley cells to vary by setting the constraint on the AM-conserving zonal wind to

$$u = \Omega a \left[\frac{\cos^2(\phi_0)}{\cos(\phi)} - \cos(\phi) \right] = \Omega a \left[\frac{\mu_0}{\cos(\phi)} - \cos(\phi) \right] \tag{16}$$

where ϕ_0 is the latitude of rising motion separating the two Hadley cells and $\mu_0 = \cos^2(\phi_0)$. Combining this with (14), using both the small-angle approximation and the quadratic

formula, we find

$$\phi^2 = \frac{1 - \mu_0}{2\mu_0} \pm \sqrt{\left(\frac{1 - \mu_0}{2\mu_0}\right)^2 + \frac{g\Delta_v H_T}{\Omega^2 a^2 \mu_0}} \qquad (17)$$

where the positive root must be taken to ensure a non-imaginary edge latitude.

The modified *Held* (2000) scaling relationship in (17) allows us to explore the seasonal cycle of the edge latitudes and width of the Hadley cell in an idealized context by varying the latitude of rising motion, the fractional dry stability, and the tropopause height. The latitude of rising motion is parameterized to follow the seasonal cycle of the latitude of the Intertropical Convergence Zone (ITCZ) described in *Waliser and Gautier* (1993). The ITCZ is modeled to have a seasonal cycle amplitude of 8 degrees latitude, shifted 2 degrees north to produce a Northern Hemisphere bias, with the function's "shape" set by the declination angle, i.e. $\phi_0 = 8° \cos(2\pi(N + 9)/365) + 2°$ where N is the Julian day. The resulting ITCZ latitude is shown in Figure 4a.

The height of the tropical tropopause exhibits an annual seasonal cycle of temperature, pressure, and height, with low tropopause heights in boreal summer and high heights in boreal winter (*Reid and Gage*, 1981). It is similarly parameterized with the shape of the declination angle with a seasonal cycle amplitude of 500 m about an average height of 16.5 km, i.e. $H_T = 500m \times \cos(2\pi(N + 9)/365) + 16.5 \times 10^3 m$, plotted in Figure 4b.

Lu et al. (1) (2007) found that the width of the Hadley circulaton in model simulations run for the CMIP3 was far more correlated with the extratropical rather than tropical fractional stability through the *Held* (2000) scaling relation. The dry stability in the subtropics and extratropics at the poleward boundaries of the tropical belt in each
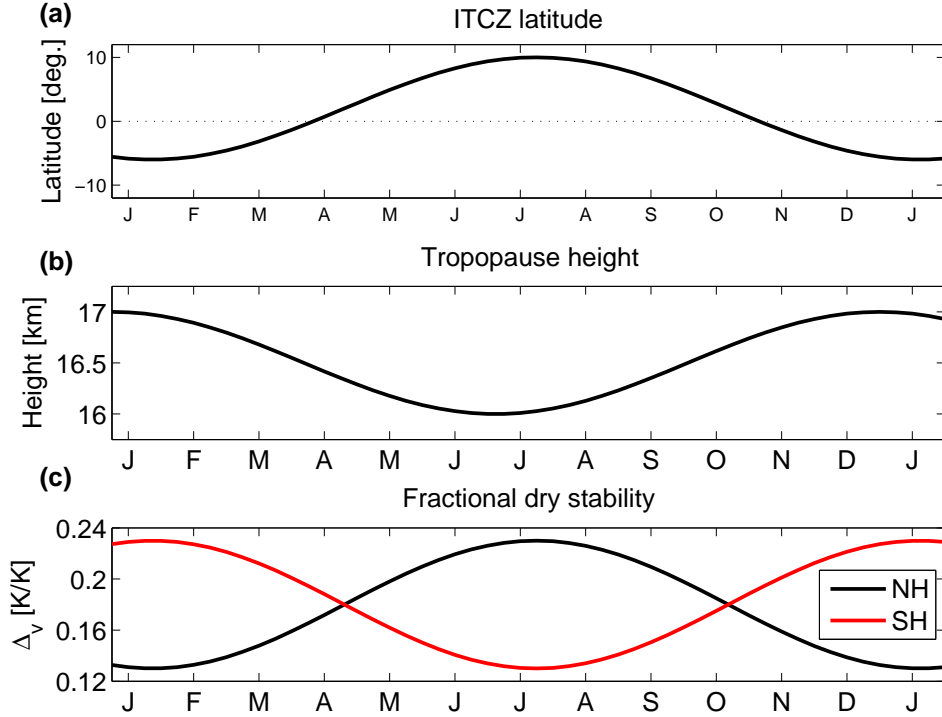
Figure 4: Parameterized seasonal cycles of (a) ITCZ latitude, (b) tropopause height, and (c) fractional dry stability for the modified *Held* (2000) model. See text for further information.

hemisphere reaches a minimum in the winter and maximum in the summer (*Frierson and Davis*, 2011), hence we will model the dry stability as peaking in the summer. From the definition of Δ_v, increasing dry stability between the tropopause and surface increases the fractional dry stability. For typical, annual-mean tropical tropopause and surface potential temperatures of 370 K and 310 K, the fractional dry stability is $\Delta_v = 0.18$. The fractional dry stability is thus parameterized, also using the shape of the declination angle, as

$\Delta_v = \delta \times 0.05 \times \cos(2\pi(N+9)/365) + 0.18$, where $\delta = 1$ for the Northern Hemisphere and $\delta = -1$ for the Southern Hemisphere. Both the Northern and Southern Hemisphere fractional dry stabilities are shown in Figure 4c.

The resulting seasonal cycle of Northern and Southern Hemisphere edge latitudes and the full tropical belt width are shown in Figure 5, for both the cases of constant ("constant

parameters") Δ_v and H_T, varying fractional dry stability and constant H_T ("varying stability"), and varying tropopause height with constant Δ_v ("varying tropopause height"). The semi-annual seasonality of the edge latitudes, most apparent for the model with constant tropopause height and dry stability, is modulated by the displacement of the ITCZ from the equator. In the model, the ITCZ latitude sets the initial angular momentum in the poleward-flowing branches of the Hadley cells. Thus, when the ITCZ is most displaced from the equator, the initial angular momentum is lower and hence the flow can extend most poleward in both hemispheres. In other words, the edge latitudes go as $|\phi_0|$.
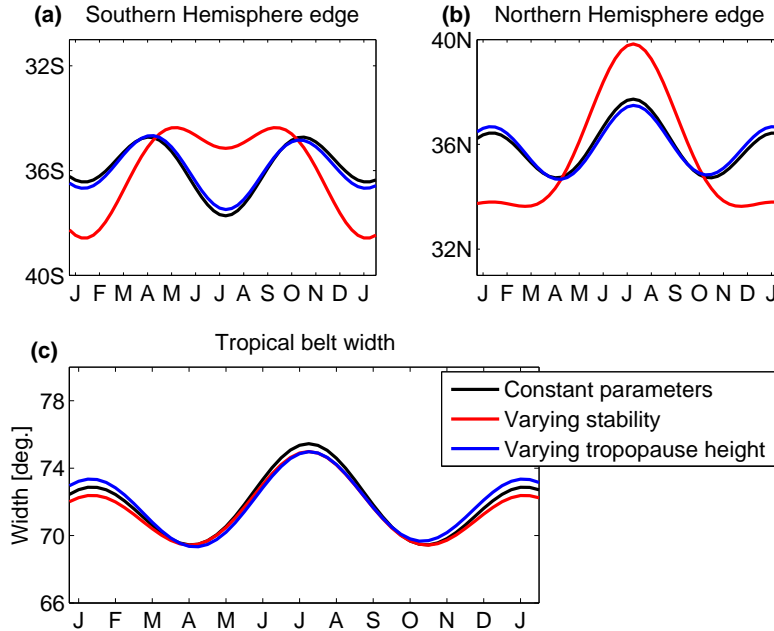
Figure 5: Seasonal cycle of the (a) Southern Hemisphere and (b) Northern Hemisphere Hadley cell edge and subtropical jet latitudes and (c) total tropical belt width based on the modified *Held* (2000) model. The black curve uses constant values of $H_T = 16$ km and $\Delta_v = 0.18$, while the red (blue) curve uses the parameterized seasonal cycle of Δ_v with $H_T = 16$ km (H_T with $\Delta_v = 0.18$) described in the text. Both models use the parameterized ITCZ latitude ϕ_0, also described in the text.

Without allowing the dry stability and tropopause height to vary, both hemispheres exhibit roughly the same edge latitude seasonality, with the minor differences arising from

the Northern Hemisphere bias of the ITCZ. Allowing the tropopause height to vary, but keeping the fractional dry stability constant, produces results nearly indistinguishable from the case of constant parameters. We thus conclude that tropopause height has a minimum effect on the Hadley cell extent for variations on the order of the seasonal cycle amplitude.

It is the seasonally-varying dry stability that gives the edge latitudes their hemispheric asymmetry. The deep poleward extent of the Northern Hemisphere edge latitude during boreal summer is due to the combined effect of the poleward displacement of the ITCZ and the high dry stability stabilizing the subtropical jet. The low stability in the Southern Hemisphere during boreal summer conspires to limit the poleward extent of the Hadley cell and jet, creating a local minimum in edge latitude seasonality despite the poleward displacement of the ITCZ. The sum of these and other differences does not produce an appreciably different tropical belt width compared to the model with constant parameters or a seasonally-varying tropopause height.

3.4   Variable Rossby number

Kang and Lu (2012) altered the (*Held*, 2000) Hadley cell scaling theory to account for differences in the Rossby number between the winter and summer cells using empirically derived Rossby numbers. This scaling theory attempts to account for the fact that eddies work to broaden the Hadley circulation and decelerate the jet by relaxing the flow from the AM-conserving limit (*Kim and Lee*, 2001).

However, the use of a constant, non-unity Rossby number parameterizes the effect of eddies in an obscure manner. *Kang and Lu* (2012) integrate the definition of the local

Rossby number $Ro \equiv \zeta/f$ (*Walker and Schneider*, 2006) from the latitude of rising motion to the latitude at which the Hadley cell terminates, instead of actually incorporating the effect of the eddies in (1) through the eddy stress. This scaling theory also neglected the ability of both $f + \overline{\zeta}$ and $\overline{v}$ to mediate the effects of the eddy stress on the absolute vorticity when the Rossby number is neither unity nor vanishingly small.

Further, the scaling theory loses predictive power because it isn't clear how, even in an idealized sense, the Rossby numbers in the respective cells will change as a result of anthropogenic climate forcings. A change is all but guaranteed as changes in eddy phase speeds and their resulting momentum fluxes have been observed in reanalyses (*Chen and Held*, 2007) and climate model projections of global warming (*Ceppi and Hartmann*, 2012), the latter being implicated in the poleward expansion of the Hadley cell. While simple, mechanistic arguments exist for changes to the tropopause height and dry stability, the same cannot be said for the Rossby number.

Regardless, in all of these major scaling theories for the width of the Hadley circulation, the subtropical jets emerge from the westerly accelerations induced by poleward AM-conserving flow in the upper branches of the Hadley cells, with the Hadley cell extending poleward until either the resulting jet becomes baroclinically unstable (*Held* (2000); *Kang and Lu* (2012)), or the circulation energetically closes the Hadley circulation (*Held and Hou*, 1980). We will now examine whether the latitudes of the subtropical jets and the associated latitudes of the poleward edges of the Hadley cells are as well-coupled as theory suggests.

4 Methods and diagnostics

Calculation methods for the tropopause, mean meridional streamfunction (MMS), and tropical belt width diagnostics are detailed in this section.

4.1 Tropopause

The extratropical tropopause height is typically calculated using the World Meteorological Organization (WMO) definition of the lowest height at which the lapse rate decreases to 2 K/km or less, provided the average lapse rate between this level and any higher point within 2 km does not exceed 2 K/km (*WMO*, 1957). A more appropriate definition in the tropics is to use a threshold of 0 K/km, capturing instead the so-called cold-point tropopause that represents the boundary between the tropical tropopause layer and the stratosphere. As in *Birner* (2010), the tropopause height is calculated here as the level of maximum curvature in the temperature profile, a more objective diagnostic that separates the troposphere and stratosphere by their vastly different static stabilities, and which has the advantage of capturing both the WMO and cold-point tropopauses in their respective regions. The sensitivity of this curvature method to the variability found in individual profiles does not present a problem as all tropopause values are calculated from monthly-mean, zonal-mean variables. Explicitly, the geopotential height field is interpolated onto $\partial_{zzz}T = 0$ to find the tropopause geopotential height. The tropopause temperature is found by linearly extrapolating the tropospheric lapse rate from the nearest model or data level below the tropopause to the tropopause height, and the tropopause pressure is calculated using the hypsometric equation.

4.2 Objective diagnostics

We now define the three objective diagnostics for the width of the tropical belt used in this study: the latitudes of the subtropical jet cores (denoted by U_{max}), the latitudes at which the vertically-averaged MMS vanishes (denoted by $\int \Psi dp$), and the latitudes of the maximum tropospheric dry bulk stability (denoted by $\Delta\theta$). In all three cases, the width of the tropical belt is simply the distance in degrees latitude between the Northern and Southern Hemisphere edge latitudes of each diagnostic. The diagnostics are all computed on monthly-mean, zonal-mean fields.

4.2.1 Subtropical jet (U_{max})

As previously mentioned, the subtropical jet is strongly linked to the Hadley circulation in inviscid (*Held and Hou*, 1980) and AM-conserving (*Kang and Lu* (2012) and *Held* (2000)) theories and has been previously employed to study the width of the tropical belt (*Archer and Caldeira*, 2008). However, the diagnostic employed by *Archer and Caldeira* (2008) computes the mean latitude of the mass-weighted wind over 15°-75°N in the Northern Hemisphere and thus includes contributions from both the subtropical and polar jets, the latter of which is not relevant to finding the tropical edge latitudes. While this averaging certainly reduces the variability in the estimated tropical belt width as compared to a maximum-based diagnostic (*Davis and Rosenlof*, 2012), our goal here of understanding the relationship between the different metrics for the tropical belt width necessitates measuring the precise (and perhaps highly variable) location of the subtropical jet.

Here, the latitude of the subtropical jet is defined as the latitude of the most equatorward local maximum in the zonal-mean zonal wind field in the upper troposphere and lower stratosphere (UTLS) in each hemisphere, capturing the meridional position of the subtropical jet core. We use an algorithm similar to what was used by *Strong and Davis* (2006) to find the surface of maximum wind, the pressure of the maximum zonal-mean zonal wind in the UTLS, in each grid point's column. First, each zonal-mean zonal wind column is scanned from the surface to 50 hPa above the tropopause to find the maximum column wind speed. Then, a meridional profile of the maximum wind speeds is constructed and we define the subtropical jet latitude as the latitude of the most equatorward maximum in this field in each hemisphere. Latitude is linearly interpolated onto $\partial_\phi U = 0$ to find the precise location of the jet core. To ensure that no tropical wind speed maxima are captured, we avoid searching equatorward of 15 degrees latitude. While the parameters defining the domain to be searched are necessarily subjective, the actual jet diagnostic - the zonal-mean zonal wind maximum - is objective. Like the method presented in *Strong and Davis* (2006), the primary advantage here is that the algorithm ignores the polar night jet by restricting its search to the UTLS and captures the core of the tropospheric jet.

However, if in the Southern Hemisphere the jet is found to be poleward of 45° S, we repeat the entire algorithm except instead of using the maximum column wind speed field, we use the meridional gradient of the maximum column wind speed and find the most equatorward local maximum in the region where the meridional gradient is negative (i.e., the maximum column wind speed is decreasing equatorward). We run a 2 degree latitude smoother on the maximum column wind speed field before taking the gradient and, as before, do not search equatorward of 15 degrees. This second condition captures the

"shoulder" of the zonal-mean zonal wind field in austral summer, to borrow the term from *Ceppi and Hartmann* (2012), that is in fact the subtropical jet buried among a broad distribution of upper-level westerlies. Without this additional condition, any maximum-based diagnostic will capture instead the strong Southern Hemisphere eddy-driven jet during this season. This is a drawback of any tropical belt width diagnostic based upon the subtropical jet - this jet is not well-defined in austral summer, requiring the use of this secondary condition approximately 10% of the time.

For the sake of being able to compare wind metrics between the reanalyses and GPS-RO data, we use the geostrophic wind in lieu of the observed wind to calculate the latitudes of the subtropical jets (denoted $U_{g,max}$) using the maximum column wind speed algorithm. For calculating the geostrophic wind from the reanalyses, we solve the balanced meridional momentum equation in spherical pressure coordinates,

$$fu + \frac{\tan(\phi)}{a}u^2 = -\frac{1}{a}\frac{\partial \Phi}{\partial \phi} \tag{18}$$

for u, the zonal wind, where ϕ is the latitude, Φ is the geopotential of the isobaric surface, $f = 2\Omega \sin(\phi)$ is the Coriolis parameter where $\Omega = 7.292 \times 10^{-5}$ s^{-1} is the rotation rate of the earth and $a = 6,371$ km is the mean radius of the earth. The metric term $u^2 \tan(\phi)/a$ is included because at wind speeds commonly found in the subtropical jet, the term is on the order of 5% of the Coriolis term fu, a non-negligible contribution when trying to precisely locate the jet core. To calculate the geostrophic wind from GPS-RO data, we similarly

solve the balanced meridional momentum equation in spherical height coordinates,

$$fu + \frac{\tan(\phi)}{a}u^2 = -\rho^{-1}\frac{1}{a}\frac{\partial P}{\partial \phi} \qquad (19)$$

for u, where ρ is the dry air density, P is the atmospheric pressure, and the other constants and variables are as before.

4.2.2 Vertically-averaged streamfunction ($\int \Psi dp$)

The MMS measures the meridional overturning circulation at a particular latitude and represents the most natural framework through which to study the Hadley cell and the width of the tropical belt. The MMS is calculated as the vertical integral of the mass-weighted zonal-mean meridional wind between the top of the atmosphere and each pressure level (*Holton*, 1994), given by

$$\Psi(\phi, p) = \frac{2\pi \cos(\phi) g}{a} \int_0^p [v] dp \qquad (20)$$

where $\Psi(\phi, p)$ is the MMS at pressure level p and latitude ϕ, $g = 9.81$ m/s is the acceleration due to gravity, and $[v]$ is the monthly-mean, zonal-mean meridional wind. Previously, the tropical belt edge latitudes have been defined as the latitude at which the 500 hPa MMS (*Lu et al. (1)* (2007); *Frierson et al.* (2007)), the 600 hPa to 400 hPa average MMS (*Hu and Fu* (2007) and *Johanson and Fu* (2009)), and the 700 hPa to 400 hPa average MMS (*Stachnik and Schumacher*, 2011) vanishes poleward of its deep tropical maximum (minimum) in the Northern (Southern) Hemispheres, calculated from seasonal-

and annual-mean data. To produce a more objective measure of the Hadley circulation's width, in this study the MMS is vertically-averaged in pressure over the full depth of the atmosphere, and the tropical belt edge latitude is then defined as the location where the vertically-averaged MMS vanishes, poleward of its deep tropical maximum (minimum) in the Northern (Southern) Hemisphere. Latitude is linearly interpolated onto $\int \Psi dp = 0$ to find the vanishing location between grid points.

Averaging up to the tropopause produces results indistinguishable from averaging over the depth of the atmosphere; the magnitude of the MMS is small above the tropopause and most of the mass in an atmospheric column is in the troposphere. This averaging method becomes advantageous on the monthly timescales studied herein, as the zero-contour of the MMS can develop significant meridional undulations across different pressure levels during the spring and fall months, such that one can obtain significantly different tropical belt widths depending upon the level chosen.

4.2.3 Maximum tropospheric dry bulk static stability ($\Delta\theta$)

Finally, we introduce a new tropopause-based objective diagnostic for the tropical edge latitudes: the latitudes of the maximum tropospheric dry bulk static stability, hereafter bulk stability. The bulk stability is defined here as the total difference in potential temperature between the tropopause and the surface and represents a simple measure of stability within a layer irrespective of thickness, as opposed to static stability which measures the local stratification. As noted in *Frierson and Davis* (2011), there is a distinct and unambiguous subtropical maximum in both the bulk and vertically-averaged static stabilities in both hemispheres occuring in the subtropics near the subtropical tropopause

30

break, the structure of the bulk stability being primarily a function of the meridional temperature structure of the tropical cold-point tropopause (*Seidel et al.*, 2001). Calculation of the bulk stability only requires the surface and tropopause potential temperatures and a simple subtraction operation, as opposed to the more complicated vertical-averaging and finite-differencing required to calculate the vertically-averaged static stability. The edge latitude is thus simply defined as the latitude of the maximum tropospheric bulk stability in each hemisphere. 2-meter temperature and surface pressure are used to calculate the surface potential temperature from the reanalyses, whereas the previously-discussed GPS-RO surface fields are used to calculate the surface potential temperature. Quadratic interpolation onto a 0.1° latitude grid is used to estimate the latitude of the maximum between grid points. This diagnostic presents the best opportunity for evaluating the reanalyses' tropical belt widths as it is entirely temperature-based and can be compared with GPS-RO data.

A sample of monthly-mean and the annual-mean bulk stabilities from 1999 derived from ERA-i is shown in Figure 6 to illustrate both the well-defined nature of the subtropical maximum and its persistance throughout the seasonal cycle. While the subtropical maximum in the annual mean is still sharply defined, the width of 53 degrees based on the annual-mean profile is notably narrower than the width of 60 degrees based upon the mean of the monthly-mean widths. Figure 7 plots a time series of Northern and Southern Hemisphere edge latitudes for this diagnostic, including edge latitudes obtained from CHAMP and COSMIC, over the 2001-2011 period. The structure of the edge latitudes' seasonal cycles and their variability will be analyzed in the proceeding sections.
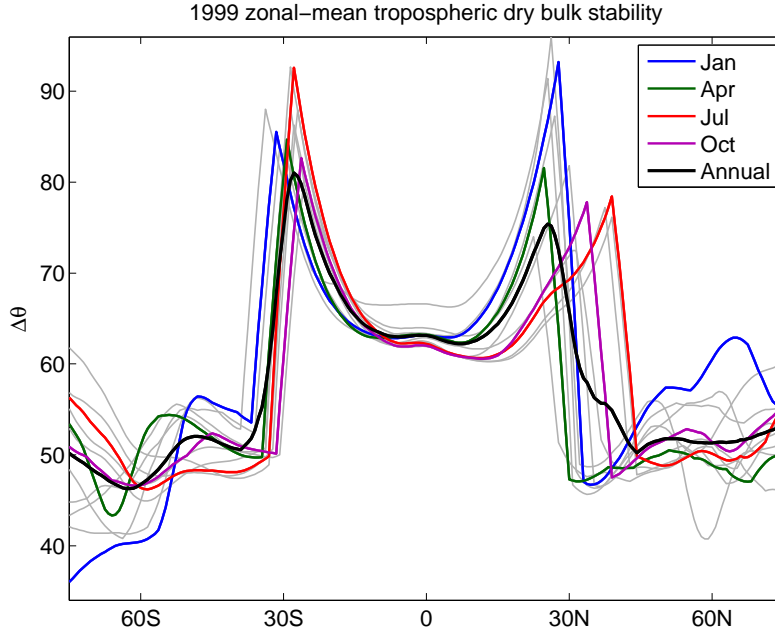
Figure 6: Annual-mean (black), January (blue), April (green), July (red), October (purple), and the remaining monthly-mean (grey) zonal-mean tropospheric bulk stabilities derived from ERA-i for 1999.
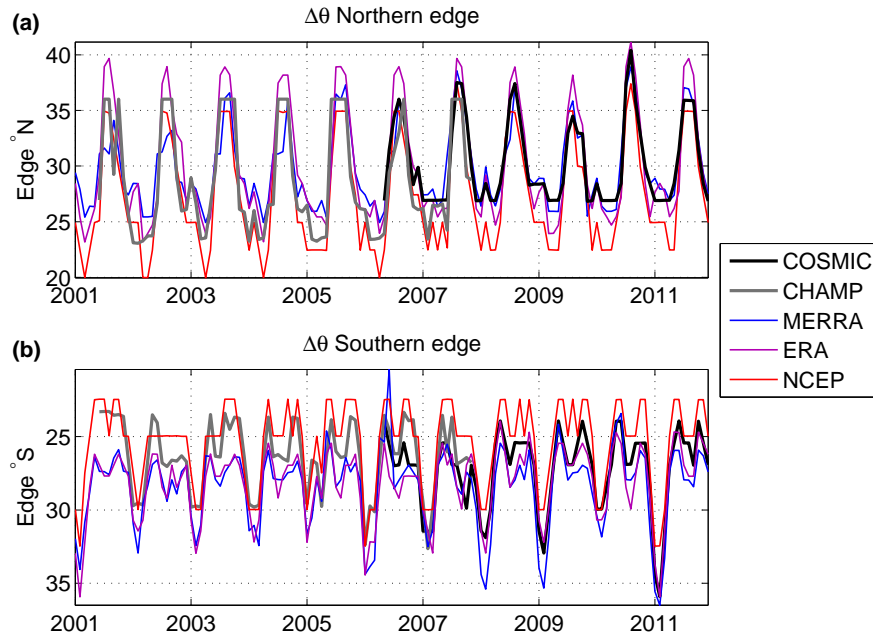
Figure 7: Time series of (a) Northern and (b) Southern Hemisphere tropical belt edge latitudes for the $\Delta\theta$ diagnostic, with edge latitudes from COSMIC (black), CHAMP (grey), MERRA (blue), ERA-i (purple), and NCEP (red), for the 2001-2011 time period when GPS-RO coverage is available.

5 Results

5.1 Seasonal cycle

5.1.1 Full tropical belt width time series

The time series of each of the monthly-mean tropical belt widths obtained via the three diagnostics - the latitudes of the maximum tropospheric bulk stability ($\Delta\theta$), the latitudes of the subtropical jet cores (U_{max}), and the latitudes at which the vertically-averaged MMS vanishes ($\int \Psi dp$) - are plotted in Figure 8. Trends in the different diagnostics will be discussed later. Throughout this paper, a standard color scheme of blue, purple and red correspond to MERRA, ERA-i, and NCEP, respectively, when presenting data from more than one reanalysis product. COSMIC and CHAMP $\Delta\theta$ widths are plotted in black and grey, respectively, for the years in which they have coverage.

The different diagnostics all display a broadly consistent seasonality between reanalyses, with a clear annual maximum and minimum and a seasonal cycle amplitude on the order of 10 degrees latitude. $\Delta\theta$ widths display a consistent offset between reanalyses throughout the period of analysis, although they qualitatively appear to converge later in the series around 2005. The U_{max} widths are remarkably consistent between reanalyses, and the time series are essentially coincident except for a few months, notably in 1986 and 1999, with correlation coefficients between reanalysis time series in excess of 0.97. MERRA appears to consistently produce narrower $\int \Psi dp$ widths in the boreal spring months relative to the other reanalyses, and NCEP produces anomalously wide $\int \Psi dp$ widths in 1993 and 1996 that are not reproduced in either MERRA or ERA-i.
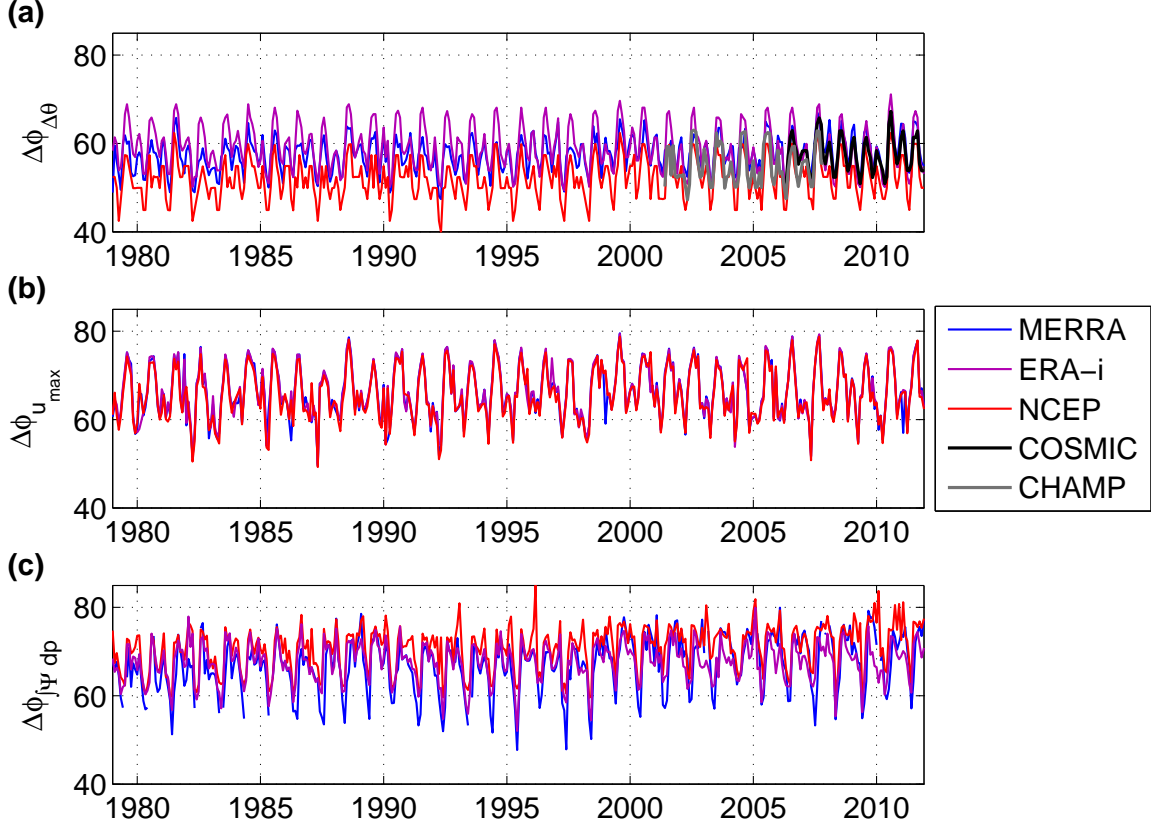
Figure 8: Time series of monthly tropical belt widths for the (a) $\Delta\theta$, (b) U_{max}, and (c) $\int \Psi dp$ diagnostics derived from MERRA (blue), ERA-i (purple), NCEP (red), COSMIC (black), and CHAMP (grey).

5.1.2 Climatological-mean seasonal cycle

Figure 9 displays the seasonal cycle of the tropical belt edge latitudes and widths derived from ERA-i for each of the three diagnostics as well as the $\Delta\theta$ diagnostic derived from COSMIC, all averaged over the period 2007-2011 for comparison with COSMIC. The seasonal cycle is similar for the full 1979-2011 period, with minor differences in the mean width. Examining the seasonal cycle of the edge latitudes, we find that the Northern Hemisphere edge has a larger seasonal cycle amplitude than that of the Southern Hemisphere, with a poleward excursion out to 45N in the U_{max} diagnostic. This difference in amplitude provides some insight into why all of the diagnostics suggest that the

July-August-September (JAS) maximum in the tropical belt width is larger than the January-February-March (JFM) maximum: the maximum in width during each hemisphere's winter season is primarily due to the deep poleward excursion of the opposite hemisphere's edge latitude, with this excursion being larger in austral winter than boreal winter.
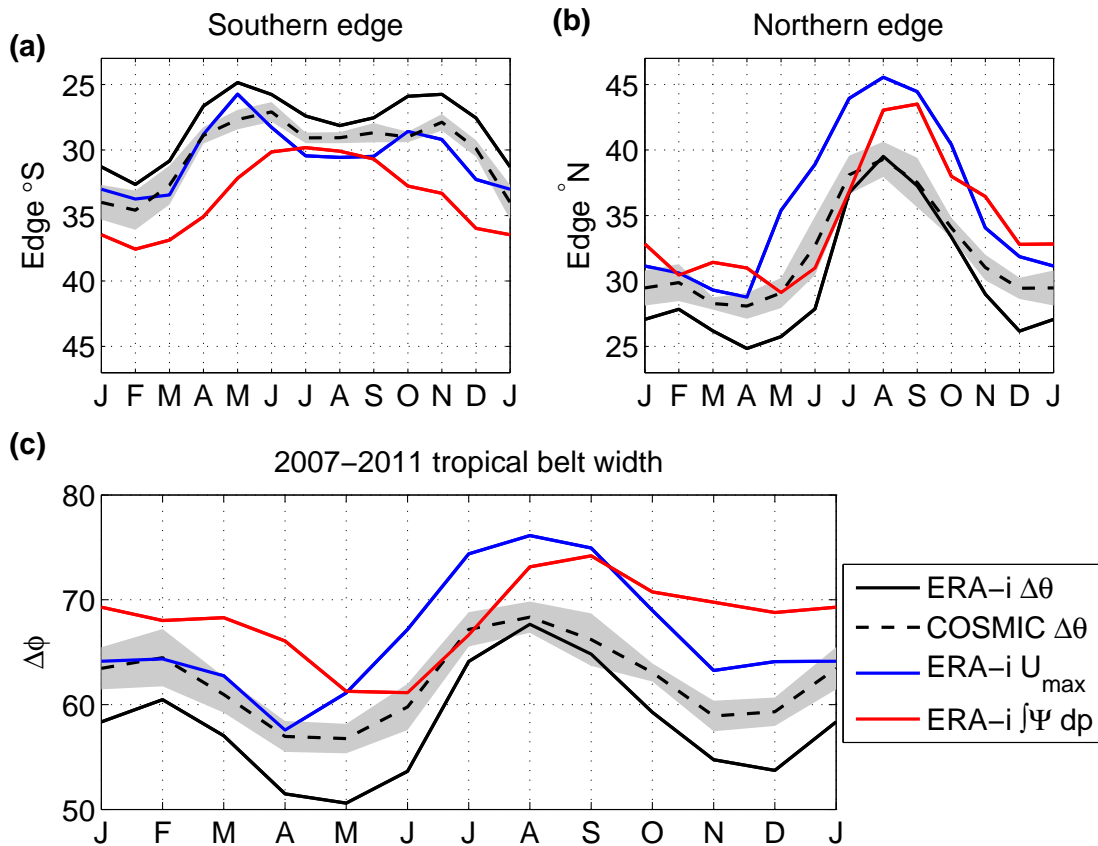
Figure 9: The seasonal cycle of (a) Southern and (b) Northern Hemisphere edge latitudes and (c) tropical belt widths (in degrees latitude) derived from ERA-i (solid) and COSMIC (dashed), for the $\Delta\theta$ (black), U_{max} (blue), and $\int\Psi dp$ (red) diagnostics. The shading on the COSMIC $\Delta\theta$ edge latitudes and width denotes the $\pm2\sigma$ bounds.

The most basic feature of the seasonal cycle of the tropical belt width is its 6-month period, with two maxima in JFM and JAS, and corresponding minima in April-May-June (AMJ) and October-November-December (OND). The former are consistent with the wide

solsticial Hadley cell that results from off-equator heating (*Lindzen and Hou*, 1988). Notably, the $\Delta\theta$ edge latitudes and widths derived from ERA-i fall below the 95% confidence interval of the $\Delta\theta$ edge latitudes and width derived from COSMIC in April through June and November through January, suggesting that the observed seasonal cycle amplitude of this tropical belt width diagnostic is weaker than that simulated in the reanalyses. Additionally, the $\Delta\theta$ diagnostic derived from both COSMIC and ERA-i does not exhibit as pronounced a maximum in its width in JAS as exhibited by U_{max}, primarily associated with the latter's Northern Hemisphere edge latitudes in JAS extending five degrees farther poleward than the $\Delta\theta$ edge latitude.

These features of the edge latitudes' seasonal cycles are not artifacts of averaging but are instead persistant features of the seasonal cycle, as illustrated in Figure 7 for the case of the $\Delta\theta$ diagnostic. For example, the slight poleward excursion in the Southern Hemisphere edge latitude during austral winter is present in the time series every year and in nearly every data set.

While the seasonal cycle of the $\Delta\theta$ and U_{max} edge latitudes and widths are comparable, this is not the case for the $\int \Psi dp$ diagnostic. The nuanced structure of the Southern Hemisphere edge latitude, with a local maximum in poleward extent in JAS, is absent in the $\int \Psi dp$ edge latitude. Instead, $\int \Psi dp$'s Southern Hemisphere edge latitude displays a simpler structure with one maximum and one minimum in poleward extent. As a result, the $\int \Psi dp$ width has a more basic structure with a single minimum in width in May and June and a single maximum in September, both lagging the minima and maxima of the other diagnostics by approximately one month, along with an amorphous structure in November through March without any noteworthy local maximum.

It is somewhat surprising to see that the seasonal cycle of edge latitudes and the tropical belt width from the idealized scaling theory (Figure 5) reproduces the observed seasonal cycles of the same for both the subtropical jet and the tropopause break. The weaker seasonal cycle amplitude in the Southern Hemisphere edge latitude and the general "shape" of each hemisphere's edge latitudes are consistent with those in the model, as is the semi-annual seasonal cycle of the tropical belt width. The primary differences are in the timing of the maxima and minima and the seasonal cycle amplitude, with the maximums and minimums ocurring later (perhaps due to thermal inertia and a non-instantaneous adjustment time) and a tropical belt width amplitude nearly three times as large.

5.1.3 Climatological-mean phase relationships

Figures 10a-10c compare the evolution of the seasonal cycle between the three diagnostics using the full 1979-2011 linear-least-squares-detrended climatological-mean monthly tropical belt widths. Only ERA-i is shown as plots are similar for both MERRA and NCEP.

Figure 10a shows that U_{max} and $\Delta\theta$ have a linear relationship between their widths throughout the seasonal cycle, and while the $\Delta\theta$ widths are offset, tending to be narrower than the U_{max} widths throughout the seasonal cycle, they clearly share a similar seasonal cycle amplitude. On the other hand, Figures 10b and 10c illustrate the markedly different seasonal behavior between the $\int \Psi dp$ and the $\Delta\theta$ and U_{max} widths, with $\int \Psi dp$ having a clearly lower seasonal cycle amplitude than the other diagnostics, as the boreal/austral winter peak width asymmetry observed in the other diagnostics is not observed as strongly in $\int \Psi dp$. Additionally, the annular structure of the seasonal cycle evolution is evidence of
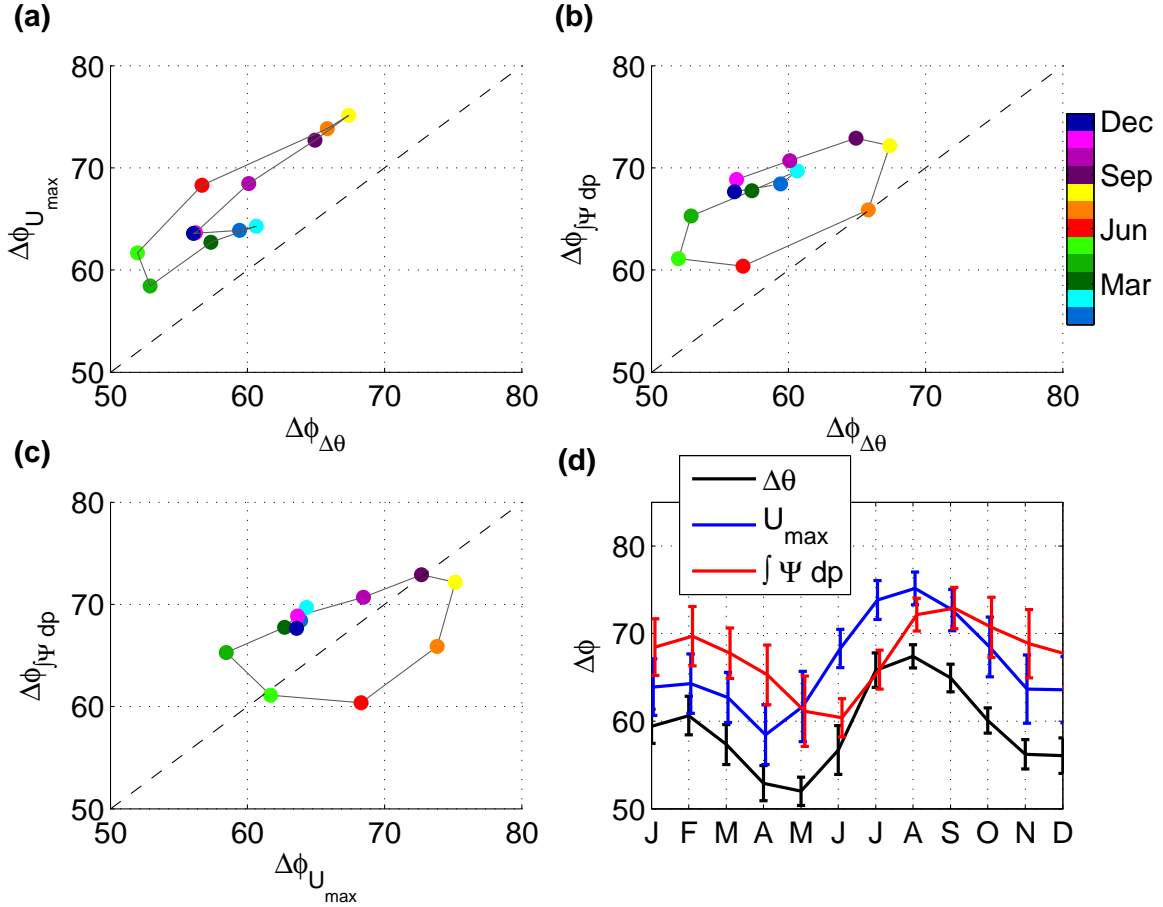
Figure 10: Seasonal progression of the monthly-mean tropical belt widths comparing (a) U_{max} vs. $\Delta\theta$, (b) $\int \Psi dp$ vs. $\Delta\theta$, and (c) $\int \Psi dp$ vs. U_{max} derived from ERA-i, with 1:1 lines in dashed black. Blues, greens, reds, and purples correspond to DJF, MAM, JJA, and SON. Months within each season progress from darker to lighter hues and are connected by grey lines. The seasonal cycle of tropical belt widths for $\Delta\theta$ (black), U_{max} (blue), and $\int \Psi dp$ (red) with 1σ bars are plotted in (d).

a phase shift in the seasonal cycle of $\int \Psi dp$ relative to the other diagnostics, with the shift

occurring between March and September when the climatological means depart from their

more linear relationship.

The tropical belt width and Northern Hemisphere edge of the subtropical jet lead the

Hadley cell edge in its climatological-mean progression by approximately one month.

The seasonal structure of $\int \Psi dp$ is notably different than those of $\Delta\theta$ and U_{max}, as well, warranting a further investigation of the diagnostics beyond the seasonal cycle.

5.2 Interannual variability

The $\int \Psi dp$ diagnostic is clearly different from the U_{max} and $\Delta\theta$ diagnostics in terms of the seasonal cycle, though the difference turns out to be more subtle with respect to the tropical belt width response to the El Niño-Southern Oscillation (ENSO), specifically the Niño 3.4 index.

5.2.1 El Niño-Southern Oscillation

The monthly Niño 3.4 sea surface temperature (SST) anomalies as described in *Trenberth* (1997) are the area-averaged SST anomalies between $120° - 170°W$ and $5°S - 5°N$ that measure the phase of ENSO, the quasiperiodic variation in sea surface temperatures in the tropical Pacific Ocean. El Niño can affect the tropical belt width by intensifying the subtropical jet via thermal wind adjustment. As a consequence of the increased wind speeds on the tropical flank of the jet, waves with a given phase speed can penetrate deeper into the tropics, the result being an equatorward shift of the momentum flux convergence field and hence the subtropical jet core (*Lu et al. (2)*, 2008). ENSO also weakens the subsiding branches of the Hadley circulation. In both cases the result is an equatorward contraction of the tropical belt (*Lu et al. (1)*, 2007).

Figure 11 displays the lag correlation (left column) and lag regression (right column) coefficients between the Niño 3.4 index and the deseasonalized tropical belt width time series of all three diagnostics derived from each reanalysis. The lags run from -24 to $+24$ months, with positive lags indicating the tropical belt width lagging the Niño 3.4 index. Correlations transition to positive values beyond approximately ± 12 months as ENSO typically oscillates between positive and negative phases on this timescale. Given the short length of the GPS-RO records, they are excluded from this analysis.
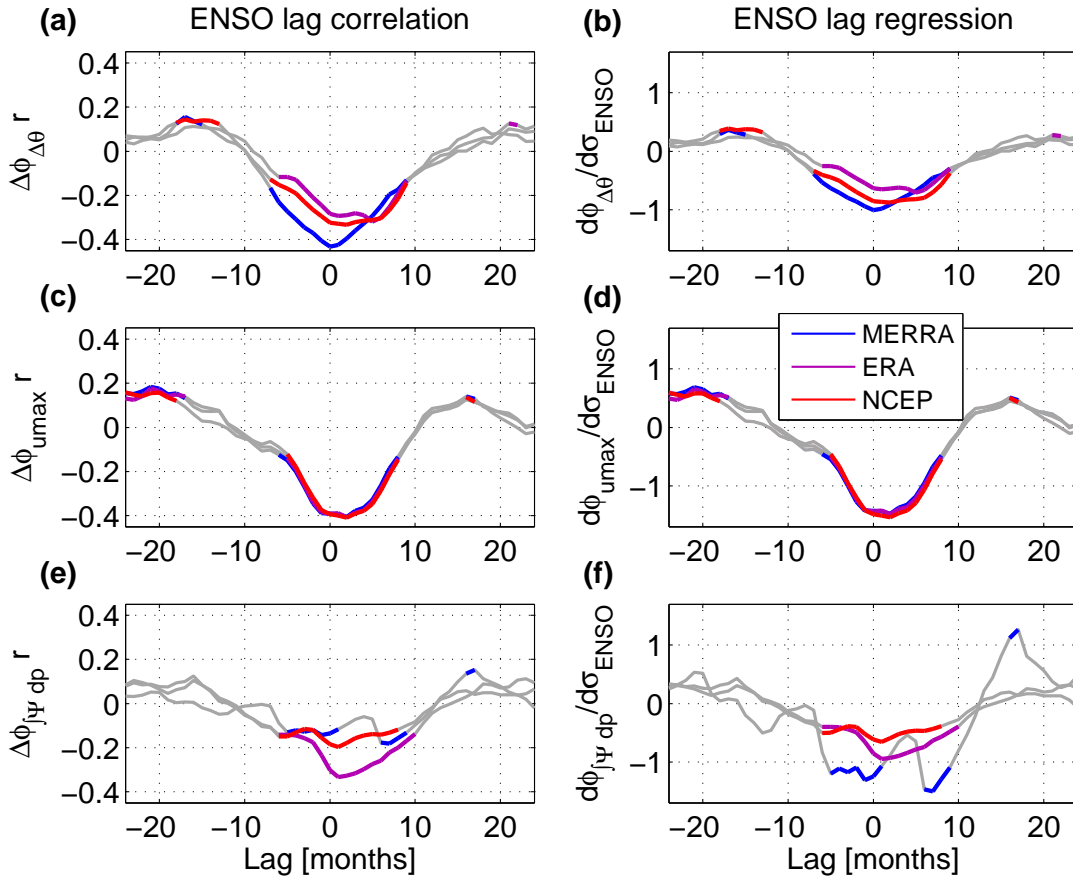
Figure 11: Lag correlations (left column) and lag regressions (right column) between the Niño-3.4 index and the deseasonalized (a) $\Delta\theta$, (b) U_{max}, and (c) $\int \Psi dp$ tropical belt widths derived from MERRA (blue), ERA-i (purple), and NCEP (red). Lag correlations span -24 to +24 months, with a positive lag indicating the tropical belt width lagging Niño-3.4. Correlation and regression coefficients not significant at the 95% level are shaded grey.

The lag correlations are qualitatively consistent between the reanalyses within the same diagnostic, with differences of less than 4 months for the lag time of zero correlation (at -9 and $+16$ months for $\Delta\theta$, for example). However, the reanalyses display the weakest consistency in the $\int \Psi dp$ width's time of peak (anti)-correlation with ENSO, with a noisy correlation structure ranging between -0.1 and -0.3 during the -10 and $+10$ month period. In contrast, both the $\Delta\theta$ and U_{max} correlations display an unambiguous and statistically significant minimum of between -0.3 and -0.4 around the 0 month lag.

These are lower by nearly a factor of two than the correlations between ENSO and the tropical belt width found in *Birner* (2010), although this may in part be due to the use of annual-mean values in the latter, as the monthly-mean widths studied here may be more influenced by other higher-frequency modes of variability. Using the annual-mean Niño 3.4 index and annual-mean tropical belt widths, both U_{max} and $\Delta\theta$ exhibit a correlation of -0.7, in agreement with the results of *Birner* (2010), whereas $\int \Psi dp$ exhibits a comparatively lower correlation of -0.3. Even on annual timescales, the ENSO response of $\int \Psi dp$ is markedly different from the other diagnostics.

While the lag correlations for U_{max} and $\Delta\theta$ are similar, the magnitude of their tropical belt width response to ENSO differs. The lag regression coefficients for $\Delta\theta$ peak at between -0.6 and -1 deg/σ_{ENSO}, whereas the U_{max} diagnostics exhibits a greater sensitivity to ENSO, peaking at -1.5 deg/σ_{ENSO}. The lag correlations and regressions for $\int \Psi dp$ remain inconsistent between the reanalyses. The differences in magnitude and structure in the ENSO lag correlation and regression between the $\int \Psi dp$ width and the $\Delta\theta$ and U_{max} widths are subtle, with the $\int \Psi dp$ diagnostic's less robust response to and weaker correlation with ENSO perhaps reflecting its greater monthly variability.

5.2.2 Quasi-biennial Oscillation

The Quasi-biennial Oscillation (QBO) is a periodic oscillation between zonally-symmetric easterlies and westerlies situated in the tropical stratosphere (*Baldwin et al.*, 2001), with a mean period of between 28.2 (*Pawson et al.*, 1993) to 28.8 (*Maruyama*, 1997) months. The anomalies originate in the middle stratosphere at around ≈ 10 hPa and propagate downard at a rate of ≈ 1 km/month, though the downward propagation is slightly faster for the easterly anomalies (*Baldwin et al.*, 2001). The QBO is thus unique in that it is a truly periodic wave-mean flow oscillation so that its influence on the tropical belt width can be "fingerprinted" with spectral analysis.

As summarized in *Baldwin et al.* (2001), gravity, inerta-gravity, Kelvin, and Rossby-gravity waves produced by tropical convection on a range of scales propagate into the stratosphere, depositing zonal momentum and driving the zonal wind anomalies. The altitude at which the waves deposit their momentum is determined by the zonal flow itself, specifically the shear zone where a particular wave's zonal phase speed approaches the zonal wind speed (*Plumb*, 1977). The effect of the combination of waves with both easterly and westerly phase speeds is for the shear zone and thus easterly and westerly anomalies to descend in the stratosphere.

Mechanistically, the QBO exists in the tropical and not the extratropical stratosphere because the Coriolis torque is weak in the tropics. In the steady-state, momentum deposition into the tropical stratosphere cannot be balanced by the Coriolis torque via a

meridional circulation (see (1)), nor can it be damped by the resulting temperature adjustment. Instead, the momentum accelerates the zonal wind field, producing the anomalies associated with the QBO (*Scott and Haynes*, 1998).

In a similar fashion to the previous section, we perform a lag correlation between the U30 QBO index (*Naujokat*, 1986) and the deseasonalized tropical belt width time series of all three diagnostics derived from each reanalyses, shown in Figure 12. The U30 QBO index is the zonal-mean zonal wind anomaly measured at Singapore via radiosonde at 30 hPa. The QBO is essentially zonally-symmetric (*Baldwin et al.*, 2001), hence any measurement of tropical stratospheric winds will be representative of the tropics as a whole. The lags run from -24 to $+24$ months, with positive lags indicating the tropical belt width lagging the QBO index.

The zonal wind anomalies propagate slowly downward toward the troposphere, producing an apparent lag presented in Figure 12 between the QBO and the tropical belt width. The height of the 30 hPa surface in the deep tropics is approximately 24 km, while the tropical tropopause height is typically 16 km. The expected apparent lag would be 8 months given a descent rate of 1 km/month, assuming the QBO's maximum effect on the tropical belt width occurs when it reaches the troposphere. Thus, the 8-month lag is close to the 0-month lag relative to when the QBO reaches the tropopause.

The only significant correlation structure is found with the tropopause-based $\Delta\theta$ diagnostic, which has fairly weak but significant correlations centered on 8 to 9 months (a 0- to 1-month "true" lag). The sinusoidal structure across the lag correlation domain is a result of the QBO's periodicity, with a period of 28 months. There are no significant lag correlations between the QBO and the U_{max} diagnostic, and a weak, nearly non-significant
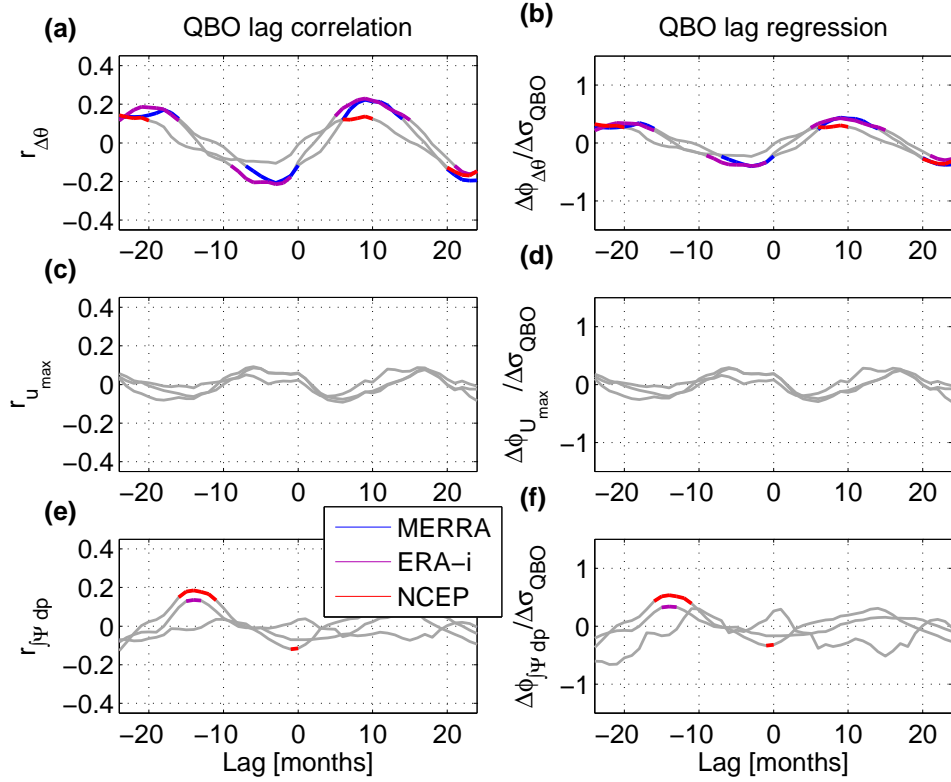
43

Figure 12: Lag correlations (left column) and lag regressions (right column) between the U30 QBO index and the deseasonalized (a) $\Delta\theta$, (b) U_{max}, and (c) $\int \Psi dp$ tropical belt widths derived from MERRA (blue), ERA-i (purple), and NCEP (red). Lag correlations span -24 to +24 months, with a positive lag of greater than $\approx$8 months indicating the tropical belt width lagging the QBO (see text for explanation). Correlation and regression coefficients not significant at the 95% level are shaded grey.

correlation structure around -14 months between the QBO and the $\int \Psi dp$ diagnostic.

Broadly, it appears that the QBO interacts with the tropopause structure, producing an anomalously-wide tropical belt width for westerly zonal wind anomalies, but does not consistently or appreciably affect the meridional location of either the subtropical jets or the edges of the Hadley cells.

To further explore the effect of the QBO on the tropical belt width, we now analyze the first empirical orthogonal function (EOF) and its associated principal component (PC) of zonal-mean dry bulk stability. Given the large difference in dry bulk stability between the

tropics and extratropics, the dominant mode of variability for this field should capture changes in the tropical belt width.

To perform the EOF analysis, the zonal-mean dry bulk stability was detrended and deseasonalized at each grid point for each of the three reanalyses. The data matrix was concatenated into an $m \times n$ matrix, where m is the number of months (396), and n the number of grid points (361 for MERRA), and was then weighted by $\sqrt{cos(\phi)}$. The $m \times m$ covariance matrix, AA^T, was then eigenanalyzed to find the eigenvectors (PC's). The original data was then projected onto the PC's to obtain their corresponding EOF's. EOF's are ranked based upon their eigenvalue, i.e., the percentage of variance that they explain. EOF significance was assessed using the method of *North et al.* (1982) and one degree of freedom per season (four per year).

The leading EOF of zonal-mean tropospheric dry bulk stability in Figure 13 derived from MERRA is dominated by hemispherically-symmetric bands at 30° N/S, suggesting that the dominant mode of tropospheric dry bulk stability variability is a symmetric pulsing of the tropical belt. The leading EOF for the other two reanalyses is qualitatively similar. The second EOF, which exhibits a greater variation between reanalyses, illustrates hemispherically-asymmetric bands in the same regions, suggesting that the second mode of tropospheric dry bulk stability variability is a meridional wobble of the tropical belt. In all three reanalyses, the first and second EOF's are significant based on the method of *North et al.* (1982).

We now analyze the power spectra of the leading PC and the U30 QBO index, shown in Figure 14. The power spectra were calculated using the discrete Fourier transform and were normalized so that the area under the curve is unity. The solid black curve is the
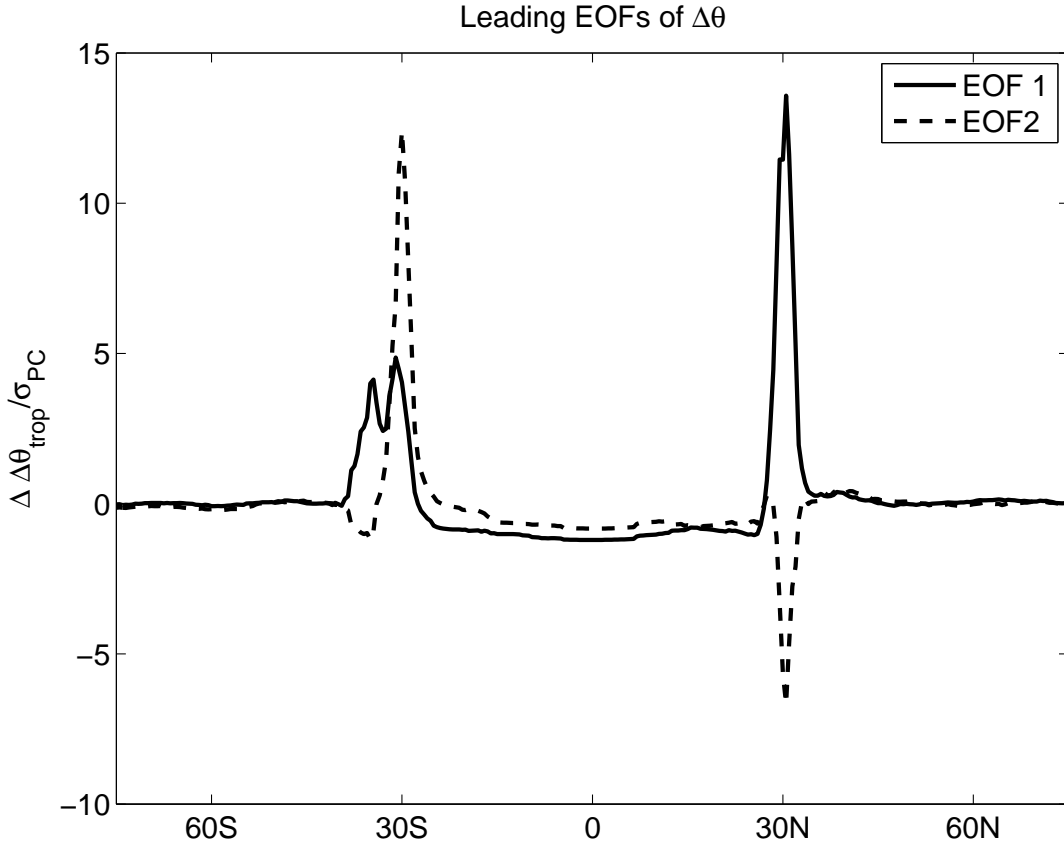
Figure 13: Leading and second EOF's of zonal-mean tropospheric dry bulk stability derived from MERRA. The EOF's are significant based on the method of *North et al.* (1982) and explain 26% and 13%, respectively, of the variance of global zonal-mean tropospheric dry bulk stability.

spectrum of the full time series, with the solid red curve the corresponding 95% significance red noise spectrum. The dashed black and red curves the same but for the subsetted data. The red noise spectra were found by calculating the autocorrelation of each time series and determining the e-folding time by interpolating $AR(\tau)$ onto $\frac{1}{e}$ in $ln(\tau)$-space, where τ is the lag. The red noise spectrum was generated using

$$\Phi(\omega) = \frac{2\tau_e}{1 + \tau_e^2 \omega^2}$$

where ω is the angular frequency in radians (2π cycles) per month. The 95% significance

level was calculated using the F-statistic for the ratio of the variance per frequency of the data to the red noise. For the non-subsetted data, there are $\nu = \frac{M}{N^*} = \frac{396}{198} = 2$ degrees of freedom per spectral estimate, where M and N^* are the time series length and number of spectral estimates, respectively, yielding an F-statistic of 3. Data was broken up into 11 overlapping subsets of length 66 months, increasing the degrees of freedom by a factor of 6 to $\nu = 12$, yielding an F-statistic of 1.7. The F-statistics were then multiplied with their red noise spectra to yield the signifance curves. The Hann window was applied to the subsetted data before analysis to reduce aliasing, and a low-pass Butterworth filter with 9 weights was used to remove unrealistic, very low-frequency components.

Examination of the power spectra in Figure 14 shows that both time series have a statistically-significant peak at a period of 28.6 months, consistent with the mean period of the QBO. In both cases the subsetted time series' peak at a period of ≈28 months is significant. This suggests that the pulsing mode of interannual variability in the width of the tropical belt, as measured by the zonal-mean tropopause structure, shares the same dominant, regular period of approximately 28 months as the QBO. The second PC, characterized by the wobbling mode of variability, shows no significant peaks in any part of the spectrum.

The mechanism by which the QBO influences the width of the tropical belt is not entirely clear. As the QBO is symmetric about the equator, the pulsing mode of variability of the tropical belt associated with the leading PC is at least consistent with some sort of symmetric QBO forcing. The ways in which the QBO influences the tropical belt width as measured by $\Delta\theta$ may be due to its associated temperature anomalies and anomalous meridional and vertical circulations.
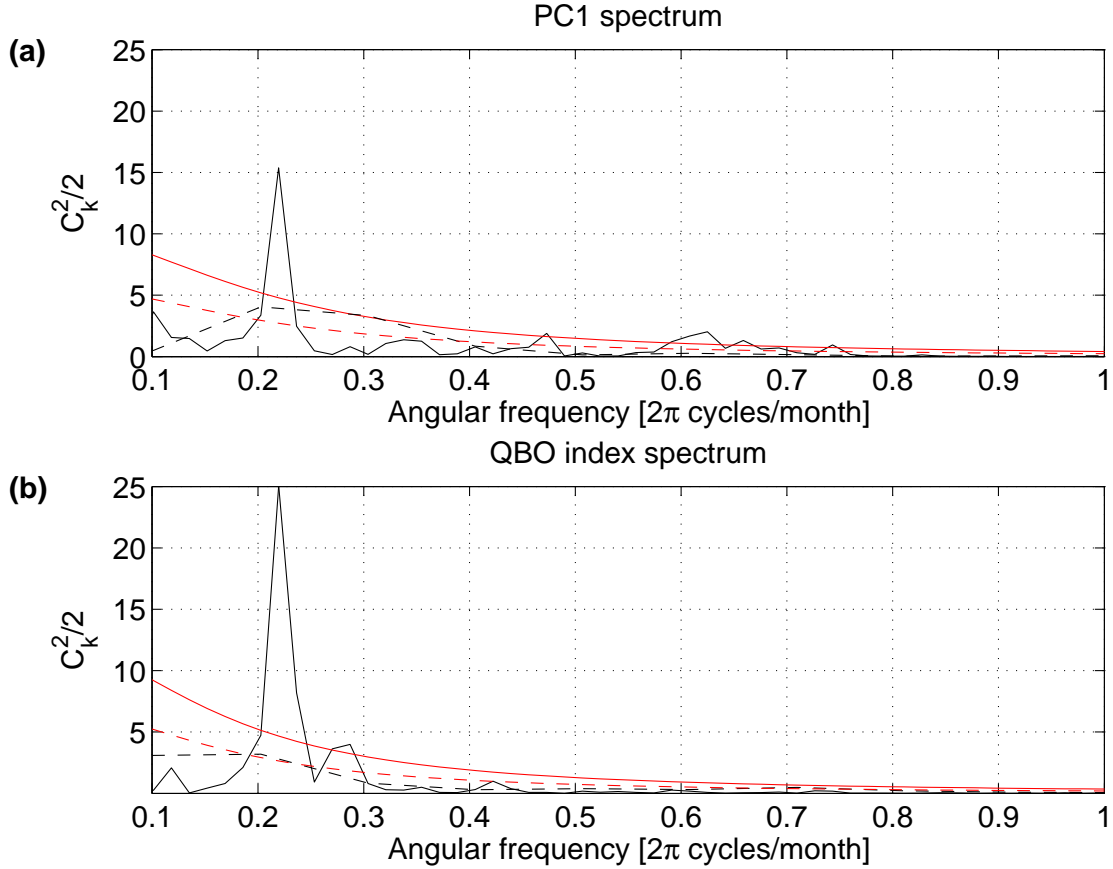
47

Figure 14: Power spectra for (a) the leading PC of zonal-mean tropospheric dry bulk stability and (b) the U30 QBO index. The solid black curve is the spectrum of the full time series, with the solid red curve the corresponding 95% significance red noise spectrum. The dashed black and red curves are the same but for the subsetted data. The maximums in both spectra correspond to a period of 28.6 months.

The schematic in Figure 15 illustrates two possible contributing mechanisms to the response. In the first case (Figure 15a), when the easterly phase of the QBO reaches the lower stratosphere it induces anomalous rising motion across the deep tropical tropopause and anomalous subsidence across the tropical tropopause at its poleward boundaries (red arrows). The resulting circulation may advect the tropopause downward at the edges of the tropical belt, eroding the poleward boundary of the tropical tropopause and leading to a contraction of the tropical belt as measured by the tropopause break diagnostic $\Delta\theta$.
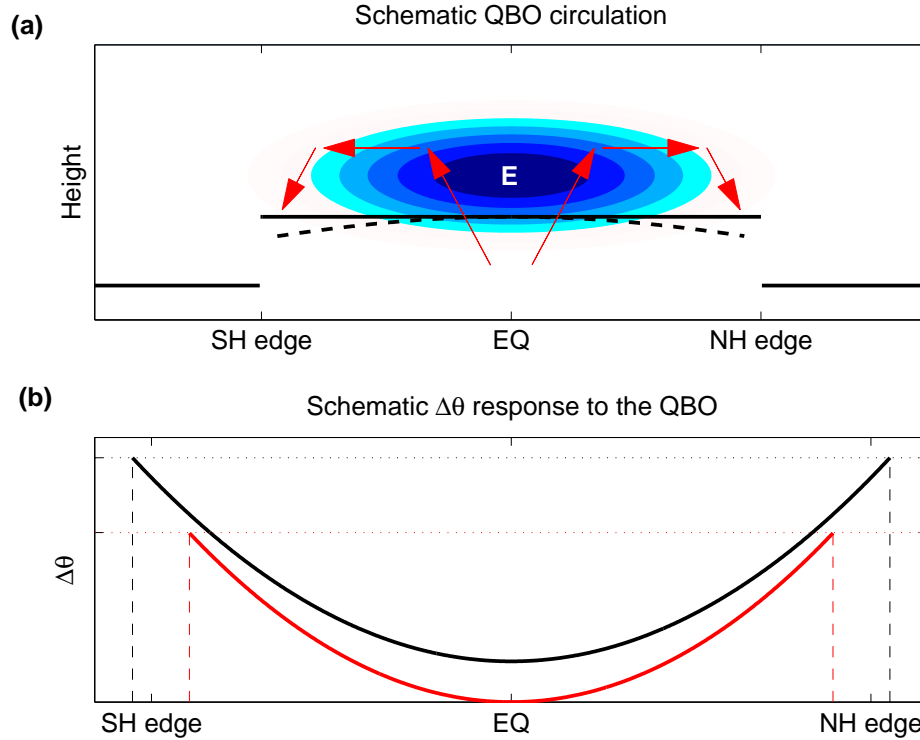
Figure 15: (a) Schematic circulation response of the tropopause to the easterly phase of the QBO. "E" denotes the easterly wind anomaly, with shading indicating its associated cold temperature anomaly. Red arrows indicate the anomalous circulations (*Baldwin et al.*, 2001). The mean-state (QBO response) tropopause is in solid (dashed) black. (b) Schematic response of the tropical belt width as measured by $\Delta\theta$ to the easterly phase of the QBO. The black line indicates the zonal-mean, time-mean dry bulk stability, while the red line indicates the zonal-mean dry bulk stability during the easterly phase of the QBO. Vertical lines indicate the edge latitudes based on $\Delta\theta$ while the dotted horizontal line indicates the critical dry bulk stability for baroclinic instability.

Another mechanism may be related to the temperature response. When the easterly phase of the QBO descends to the tropopause, it produces anomalously cold temperatures (Figure 15a, shading) at the deep tropical tropopause (*Baldwin et al.*, 2001), possibly leading to a reduction in dry bulk tropospheric stability (Figure 15b). Assuming that the subtropical jet and Hadley cell terminate at some critical dry bulk stability for which the flow becomes baroclinically-unstable, the reduction in dry bulk stability throughout the

tropics would lead to a more equatorward termination of both and hence contraction of the tropical belt.

5.3   Lag of the Hadley cell

While the $\int \Psi dp$ diagnostic's width and Northern Hemisphere edge latitudes lag those of the other diagnostics in the average seasonal cycle, the same relationship does not necessarily hold during each individual seasonal cycle in the time series. We therefore perform lag correlations between the $\int \Psi dp$ and the U_{max} and $\Delta \theta$ diagnostics' (non-deseasonalized) tropical belt widths and Northern and Southern Hemisphere edge latitudes derived from ERA-i over each seasonal cycle. The results are similar for the other reanalyses and so are omitted.

For each year, we use the January through December U_{max} and $\Delta \theta$ monthly tropical belt widths and Northern and Southern Hemisphere edge latitudes. We then use 12 months of the $\int \Psi dp$ diagnostic's monthly tropical belt widths and Northern and Southern Hemisphere edge latitudes at lags ranging from -5 months (leading U_{max} and $\Delta \theta$) to +5 months (lagging U_{max} and $\Delta \theta$). The best-fit lag for each seasonal cycle is counted as the lag which displays the highest correlation coefficient. These best-fit lags are plotted as a histogram in Figure 16. No best-fit lags were found beyond ±3 months.

The $\int \Psi dp$ diagnostic exhibits a best-fit lag correlation at +1 months for the tropical belt width in Figure 16c, showing that the pulsing of the tropical belt as measured by the streamfunction lags that measured by U_{max} and $\Delta \theta$. Examination of the individual edge latitudes shows that this lag in the tropical belt width comes primarily from the dominant
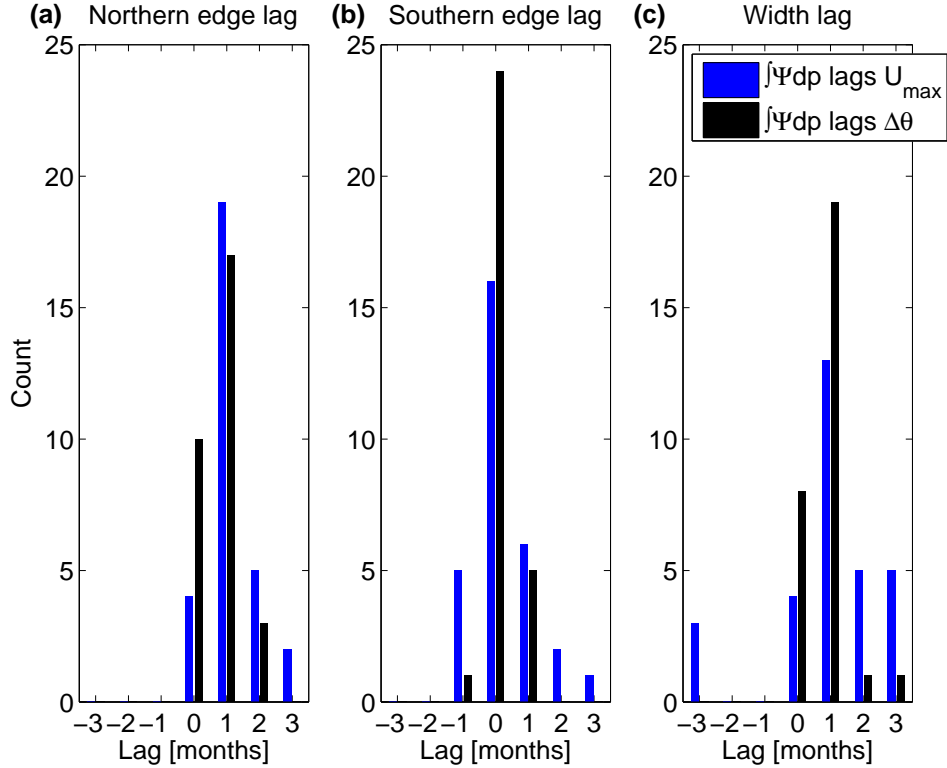
Figure 16: Histograms of the best-fit lags for each seasonal cycle between the $\int \Psi dp$ and the U_{max} and $\Delta\theta$ diagnostics for the (a) Northern Hemisphere and (b) Southern Hemisphere edge latitudes and (c) the tropical belt width derived from ERA-i. Positive lags indicate $\int \Psi dp$ lagging U_{max} and $\Delta\theta$.

1-month lag in the Northern Hemisphere edge latitudes, whereas the edge latitudes are more synchronized in the Southern Hemisphere with a best-fit lag of $\sim$0 months. These results confirm the 1-month lag seen in the average seasonal cycle of the tropical belt width and Northern Hemisphere edge latitudes.

This relationship is not limited to the vertically-integrated streamfunction. By applying the $\int \Psi dp$ vanishing latitude calculations to the streamfunction at the discrete pressure levels 500 hPa and 200 hPa, we can calculate the 500 hPa and 200 hPa edges of the streamfunction, Ψ_{500} and Ψ_{200}, respectively, in similar fashion to *Lu et al. (1)* (2007) and *Frierson et al.* (2007). Lag correlations between the $\int \Psi dp$ diagnostic and the Ψ_{500} and

Ψ_{200} diagnostics exhibit a pronounced peak at 0 months in all three reanalyses, for both the tropical belt width and the Northern and Southern Hemisphere edge latitudes (not shown). Using Ψ_{500} and Ψ_{200} produces nearly identical lag correlation histograms as presented in Figure 16, as the edges of the Hadley cell are vertically coupled on monthly timescales.

The Northern Hemisphere edge latitudes and the full tropical belt width based on the $\int \Psi dp$ diagnostic lag those based on the U_{max} and $\Delta\theta$ diagnostics by one month over the entire times series, not just in the seasonal cycle. In contrast, in the Southern Hemisphere the diagnostics are much more synchronized. This may be evidence that the Northern and Southern Hemisphere Hadley cells exist in somewhat different dynamical regimes.

5.4   Long-term trends

We now examine decadal trends based on the tropical belt width diagnostics defined in Section 4. Many studies have analyzed trends based on annual-mean tropical belt widths, but some structures in the annual mean are not representative of the mean of their monthly averages. As illustrated previously in Figure 1, the annual-mean tropospheric bulk stability is not a representative average of the monthly-mean stabilities due to its abrupt discontinuity in the subtropics averaging out to a smoother structure with a clearly narrower tropical belt width. The trends here are thus based upon deseasonalized monthly-mean values of the tropical belt width.

Figures 17a, 17b, and 17c plot the deseasonalized time series for the $\Delta\theta$, U_{max}, and $\int \Psi dp$ tropical belt widths, respectively, for MERRA, ERA-i, and NCEP. Linear least-squares trend lines are plotted as well, the details of which are listed in Table 2 which

displays the decadal trend with 95% confidence intervals, effective sample sizes, and significance for each diagnostic and reanalysis combination. Effective sample sizes were calculated using the method of *Bretherton et al.* (1999), taking into account the lag-1 autocorrelation of each deseasonalized time series. The effective sample sizes were used in determining each trend's 95% confidence interval, which was calculated using a two-tailed t-test for $\alpha = 0.05$. Trends are reported in degrees latitude per decade (deg/dec) and considered statistically significant if their 95% confidence intervals do not overlap with a trend of zero. To compare trends between different reanalyses and diagnostics, we use a two-tailed t-test evaluated at the 95% confidence level as described in *Lanzante* (2005).

The most consistent trends are found in the U_{max} widths, with trends ranging from a low of 0.3 ± 0.3 deg/dec for ERA-i to 0.6 ± 0.3 deg/dec for NCEP. The trend for the U_{max} diagnostic from ERA-i is the only trend in this analysis that is not statistically significantly different from zero at the 95% confidence level. However, the MERRA and ERA-i U_{max} diagnostic trends are not significantly different at the 95% confidence level, while the trend in NCEP is significantly different from both at the 95% confidence level (see Table 3 for these t-test results).

The widening trends ranging from 0.3 ± 0.3 to 0.6 ± 0.3 deg/dec for U_{max} in all three reanalyses are similar to the 1.6 ± 0.4 deg widening of the tropical belt based on the poleward shifts of the subtropical jet streams inferred from changes in lower stratospheric temperatures derived from the Microwave Sounding Unit (*Fu and Lin*, 2011). Over the 1979-2009 period, this widening corresponds to a linear trend of 0.5 ± 0.3 deg/dec.
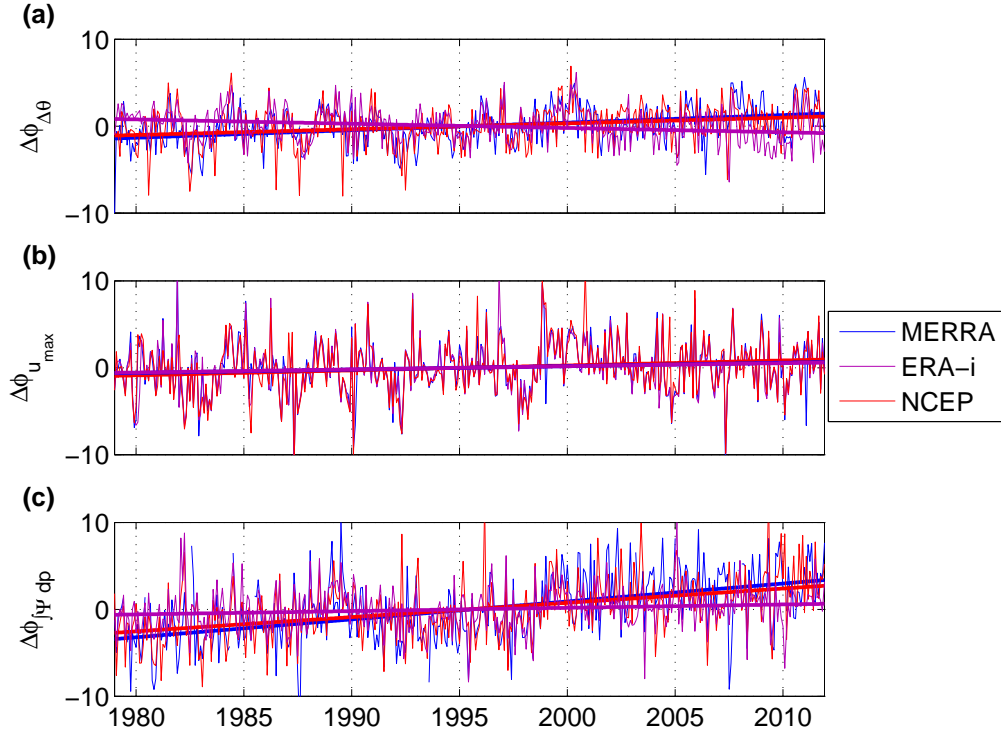
Figure 17: Time series of monthly tropical belt width anomalies for the (a) $\Delta\theta$, (b) U_{max}, and (c) $\int \Psi dp$ diagnostics and their corresponding linear least-squares regression trend lines from MERRA (blue), ERA-i (purple), and NCEP (red).

Table 2: Linear least-squares regression trends in each tropical belt width diagnostic and reanalysis in deg/dec. Trends include the 95% confidence interval. The effective degrees of freedom ν_{eff} are calculated using the method of *Bretherton et al.* (1999). Bolded trends are statistically significantly different from zero.

Metric	Trend (deg/dec)	ν_{eff}
MERRA $\Delta\theta$	**0.9 $\pm$ 0.3**	274
ERA-i $\Delta\theta$	**-0.5 $\pm$ 0.2**	329
NCEP $\Delta\theta$	**0.7 $\pm$ 0.3**	306
MERRA U_{max}	**0.4 $\pm$ 0.3**	380
ERA-i U_{max}	0.3 $\pm$ 0.3	381
NCEP U_{max}	**0.6 $\pm$ 0.3**	366
MERRA $\int \Psi dp$	**2.0 $\pm$ 0.4**	260
ERA-i $\int \Psi dp$	**0.4 $\pm$ 0.3**	334
NCEP $\int \Psi dp$	**1.6 $\pm$ 0.3**	375

Table 3: Comparison of trends between reanalyses of the same diagnostic using the two-tailed t-test as described in *Lanzante* (2005), for $[\int \Psi dp, \Delta\theta,$ and $U_{max}]$. S (NS) denotes trends (not) significantly different at the 95% confidence level.

	ERA-i	NCEP
MERRA	[S, S, NS]	[NS, NS, S]
ERA-i		[S, S, S]

In a broad sense, these trend estimates are similar to those based on the latitudes of the peak lower tropospheric wind maximum u_{850} and the mean latitudes of the mass-weighted wind $u_{400-100}$ recently reported in *Davis and Rosenlof* (2012), which are also remarkably consistent between reanalyses. It appears that the major midlatitude circulation features - the subtropical jet (U_{max}), the midlatitude jet (u_{850}), and the broad-scale zonal mass flux associated with both ($u_{400-100}$) - are unified in the magnitude of their poleward shift in the reanalyses.

ERA-i shows a negative $\Delta\theta$ width trend of -0.5 ± 0.2 deg/dec, whereas both MERRA and NCEP show significantly larger positive trends of 0.9 ± 0.3 deg/dec and 0.7 ± 0.3 deg/dec, respectively, the latter two of which are indistinguishable at the 95% confidence level. The same relationship is true of the case of the $\int \Psi dp$ diagnostic, with MERRA's and NCEP's very large trends of 2.0 ± 0.4 deg/dec and 1.6 ± 0.3 deg/dec indistinguishable from one another at the 95% confidence level and ERA-i's smaller trend of 0.4 ± 0.3 deg/dec significantly different at the 95% confidence level. It should be noted that the trends in the zero-contour of Ψ at discrete pressure levels in these data sets are comparable to their vertically-integrated $\int \Psi dp$ trend.

The $\Delta\theta$ trends are similar to those found in *Davis and Rosenlof* (2012) for the tropopause-based diagnostics z_{TP}, Δz_{TP}, and $\partial_\phi z_{TP}$, especially ERA-i's tendency toward

tropical contraction rather than expansion when specifically examining tropopause diagnostics. NCEP's $\Delta\theta$ trend of 0.7 ± 0.3 deg/dec is very similar to the trend of 0.6 ± 0.2 deg/dec derived from the same reanalysis (referred to as NCEP2) for the objective tropopause height diagnostic $z_{TP}^{t,0}$ presented in *Birner* (2010).

The trends reported here for $\int \Psi dp$ are slightly larger and have narrower confidence intervals than those found in *Davis and Rosenlof* (2012) for the zero-contour of the 500 hPa streamfunction. The narrowing of the confidence interval may be due to both the vertical averaging of $\int \Psi dp$ reducing the variability and the increase in data points from using monthly-mean widths.

In comparing different diagnostics within the same reanalysis in Table 4, we find that the majority of them are significantly different from another. Only NCEP's trends for the U_{max} and $\Delta\theta$ diagnostics and ERA-i's trends for the U_{max} and $\int \Psi dp$ diagnostics are indistinguishable from one another at the 95% level. The trends in the three diagnostics derived from MERRA are all significantly different at the 95% level.

Table 4: Comparison of trends between diagnostics within the same reanalysis using the two-tailed t-test as described in *Lanzante* (2005), for [MERRA, ERA-i, NCEP]. S (NS) denotes trends (not) significantly different at the 95% confidence level.

	$\Delta\theta$	$\int \Psi dp$
U_{max}	[S, S, NS]	[S, NS, S]
$\Delta\theta$		[S, S, S]

Ultimately, the U_{max} widths show the most consistency in the magnitude of widening between reanalyses, as compared to the $\Delta\theta$ and $\int \Psi dp$ diagnostics which display a greater range of widening between the reanalyses. ERA-i overall has the lowest trends of all the reanalyses with respect to tropical widening, with the lowest trends of the three reanalyses

in U_{max} and $\int \Psi dp$ and the outlying negative trend in $\Delta\theta$. $\int \Psi dp$ has very large trends of greater than 1.5 deg/dec of widening in MERRA and NCEP, whereas the rate of widening is smaller for $\Delta\theta$ and U_{max}. That is, even with respect to linear trends, the behavior of the Hadley cell edges and subtropical jets differ.

5.5   Reanalysis evaluation

It is unclear a priori which diagnostic nor reanalysis captures most realistically the tropical belt width and its trend. With that in mind we now employ the GPS-RO observations to test whether the reanalyses, through the U_{max} and $\Delta\theta$ diagnostics, are successfully reproducing the observed seasonal cycle and variability in the tropical belt width. Verification of trends is avoided given the short coverage period for COSMIC.

The time series of Northern and Southern Hemisphere $\Delta\theta$ edge latitudes are plotted in Figure 2 and were briefly discussed in the previous sections. The basic features of the seasonal cycle of the edge latitudes, for example the slight poleward excursion in the Southern Hemisphere edge latitude in austral winter, are persistent features in both the GPS-RO observations and the reanalyses. However, it is especially evident in the case of the boreal summer maximum in the Northern Hemisphere edge latitude that CHAMP's $\Delta\theta$ edge is "clamped" to its large grid size. As such, we will exclude CHAMP from our statistical analysis as its coverage is too sparse.

5.5.1   The geostrophic subtropical jet

While we cannot compare U_{max} from the reanalyses to observed wind data sets given the sparse coverage of upper-air observations, especially over the oceans (*Waliser et al.*,

1999), we can compare the reanalyses to COSMIC via the tropical belt widths based upon the geostrophic subtropical jet latitudes, $U_{g,max}$. As described in Section 4, the calculation of the subtropical jet latitudes is the same as U_{max}, but instead using the geostrophic wind field. Figure 18 plots the U_{max} versus $U_{g,max}$ tropical belt widths derived from the reanalyses over the 2007-2011 period, as well as their total least-squares regression lines. The regression coefficients are not significantly different from and are nearly unity, with correlation coefficients between U_{max} and $U_{g,max}$ exceeding 0.95. This is not an exceptional result as on monthly timescales and in the zonal mean, the jet should be nearly geostrophic, but this nevertheless presents a novel opportunity to study the zonal circulation using GPS-RO observations.
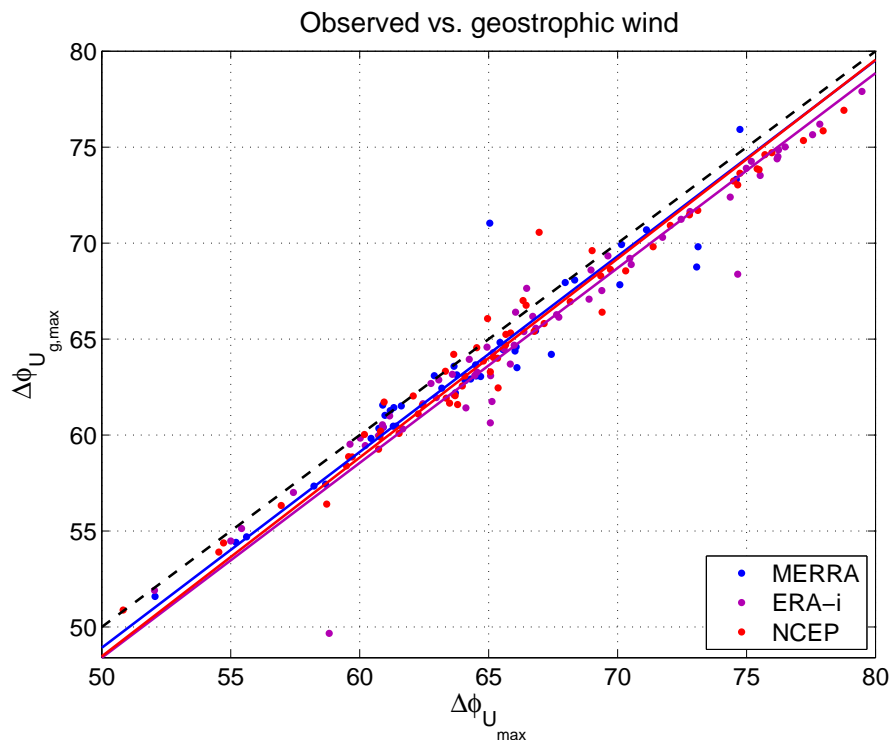

Figure 18: Monthly-mean Ug_{max} versus U_{max} widths derived from MERRA (blue), ERA-i (purple), and NCEP (red) over the 2007-2011 period. The 1:1 line is plotted in dashed black, with total least-squares regression lines plotted in each reanalyses' color scheme.

5.5.2 Evaluation with GPS-RO

The validity of the reanalyses' tropical belt widths is now determined by comparing monthly-mean tropical belt width estimates from each reanalysis with COSMIC estimates for the $\Delta\theta$ and $U_{g,max}$ diagnostics. Scatter plots of COSMIC (vertical axis) versus reanalysis (horizontal axis) monthly-mean tropical belt widths are shown in Figure 19, with the top (bottom) row corresponding to the $\Delta\theta$ ($U_{g,max}$) diagnostics, and the left (right) column corresponding to the monthly-mean (deseasonalized monthly-mean) tropical belt widths, with a 1:1 line plotted in black. The color scheme for the three reanalyses is as before, and total least-squares regression lines are plotted in each reanalyses' respective color.

As commented on earlier in the analysis of the seasonal cycle in Figure 9, the reanalyses, especially NCEP, appear to produce a narrower $\Delta\theta$ tropical belt width than COSMIC. NCEP appears to show a greater spread about the regression line, however this is clearly an artifact of its low resolution. To get a sense of how well the reanalyses capture the variability about the mean, Figure 19b shows the same tropical belt widths but with the seasonal cycle removed. Approximately half of the widths fall within the shaded region corresponding to COSMIC's grid resolution. There is some evidence of an amplitude discrepancy between the reanalyses and observations, with the reanalyses tending to produce slightly larger anomalies in a given month than COSMIC. Nevertheless, there is a strongly linear relationship between $\Delta\theta$ widths derived from the reanalyses and from observations in both the mean and anomaly sense.
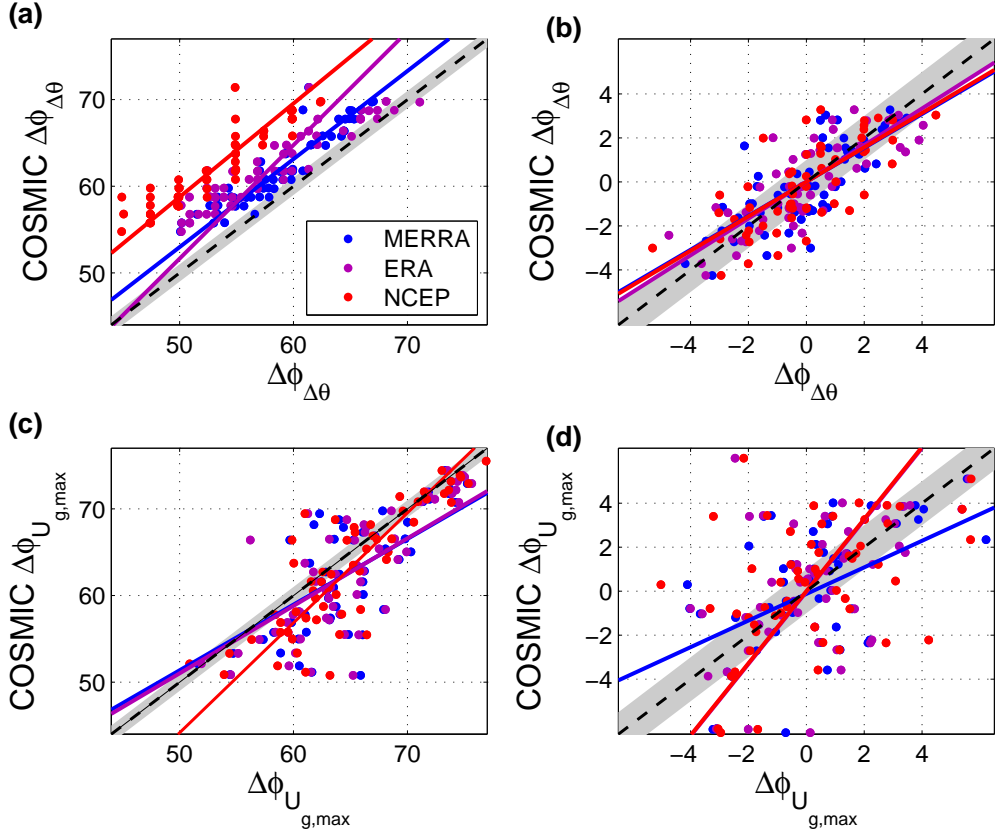
Figure 19: Scatter plots of 2007-2011 monthly mean (left column) and monthly anomaly (right column) tropical belt widths for $\Delta\theta$ (top row) and $U_{g,max}$ (bottom row) between COSMIC (vertical axis) and the three reanalysis (horizontal axis), MERRA (blue), ERA-i (purple), and NCEP (red). The 1:1 line is plotted in black and total least-squares regression lines are plotted in each data set's respective color. Shading indicates $\pm 1°$ latitude about the 1:1 line. All regression slopes are statistically significant at the 95% confidence level.

This is now contrasted with the same analysis but for $U_{g,max}$. While the monthly-mean widths are more centered on the 1:1 line than in Figure 19a, the linear relationship breaks down in Figure 19d when the seasonal cycle is removed. The frequent over- and under-estimation of the tropical belt widths in the reanalyses by as much as 3 degrees latitude, larger than COSMIC's gridded resolution, illustrates a disagreement on the position of the jet core, though it may include contributions from gridding error and locating the jet core in austral summer. Regardless, it appears that the $\Delta\theta$ width

diagnostic derived from the reanalyses more accurately reproduces the interannual

variability of the tropical belt width than the $U_{g,max}$ diagnostic.

6 Concluding remarks

6.1 Summary and implications

Existing diagnostics measuring the width of the tropical belt have been modified to be more robust on shorter timescales and have been used to examine the relationships between several different features of the general circulation in both their seasonality and in their interannual variability. The U_{max} diagnostic, a measure of the latitude of the subtropical jet core, and the $\Delta\theta$ diagnostic, a measure of the latitude of the subtropical tropopause break, exhibit a linear relationship, with similar seasonal cycle amplitudes and semi-annual seasonal cycle structures, but different seasonal mean widths. This combined with the similarity of their tropical widening trends and response to ENSO suggests a robust coupling across the timescales studied.

In contrast, $\int \Psi dp$ displays a qualitatively different seasonal cycle in its edge latitudes and width compared to U_{max} and $\Delta\theta$, with only one well-defined minimum and maximum in width and a lower tropical belt width seasonal cycle amplitude. $\int \Psi dp$'s Northern Hemisphere edge latitudes and tropical belt width also exhibit a 1-month lag relative to those of U_{max} and $\Delta\theta$, with no significant lag on monthly timescales in the Southern Hemisphere edge latitude. The latter is consistent with AM-conserving theories for width of the Hadley cell, where AM conservation in the Hadley cell and its terminating latitude due baroclinic instability essentially controls the latitude of the subtropical jet. However, if the Northern Hemisphere subtropical jet emerges from AM conservation in the poleward-flowing branch of the Hadley cell, it should be closely coupled to the edge

of the Hadley cell on monthly timescales. On the contrary, it leads the edge of the Hadley cell by one month.

These results would instead point towards the importance of extratropical influences on the Hadley circulation. *Simpson et al.* (2009) investigated the response of the general circulation to an instantaneous thermal forcing in the stratosphere, finding that broad-scale changes to the meridional circulation followed the initial response of the zonal wind. In a similar and zonal-mean sense, it may be that changes in the extratropical eddy momentum fluxes first induce changes in the zonal wind, with the meridional circulation via the Coriolis torque fv later balancing the initial perturbation. This extratropical perspective reflects the results of *Walker and Schneider* (2006) who showed that the Hadley cell strength in an idealized model was a strong function of the momentum flux divergences due to extratropical eddies. In a similar fashion, *Lu et al. (1)* (2007) found that the extratropical tropopause height, rather than tropical tropopause height, was better correlated with Hadley cell extent on decadal timescales using the *Held* (2000) scaling relation. While the Hadley cell is ultimately a response to the equator-to-pole temperature contrast (*Held and Hou*, 1980), this observational study reinforces the notion that extratropical influences on the Hadley cell cannot be neglected from a theory of the general circulation nor from Hadley cell scaling theories.

Why the $\int \Psi dp$ diagnostic exhibits a much larger widening trend than either the $\Delta\theta$ or U_{max} diagnostics is not clear. While one would be tempted to speculate that Hadley cell expansion may be decoupled from the poleward shift of the subtropical jet, the ability of the reanalyses to properly situate the zero-contour of the MMS has not been verified. It may be that ERA-i is the only reanalysis of the three studied herein that is properly

modeling this as its trend in $\int \Psi dp$ is similar to its trend in U_{max}. Regardless, as the $\int \Psi dp$ diagnostic already has the largest mean width and widening trend of the three diagnostics, if current trends continue it will become even more separated from the U_{max} and $\Delta \theta$ widths.

Finally, we examined whether the reanalyses were able to reproduce the tropical belt widths observed in GPS-RO data. Estimates of the tropical belt width based upon the $\Delta \theta$ diagnostic exhibit a linear relationship with the observed widths sourced from COSMIC observations and best capture the observed interannual variability. On the other hand, width estimates based upon the $U_{g,max}$ diagnostic, a proxy for U_{max}, do not replicate the observed interannual variability as well as $\Delta \theta$, even though the reanalyses are internally consistent in their meridional positioning of the subtropical jet core. However, the difficulty in locating the Southern Hemisphere subtropical jet in austral winter may explain some of this inconsistency. Nevertheless, out of the three diagnostics examined in this study, $\Delta \theta$ is the simplest to calculate and appears to most successfully capture the observed tropical belt width.

6.2   Future Work

There are three major avenues of future research that have been opened as a result of this study.

The mechanism by which the QBO influences the tropical belt width was only hypothesized in this study. While changes to the dry bulk stability and the anomalous vertical and meridional circulations' influence on the tropopause could qualitatively explain the expansion and contraction of the tropical belt seen during the westerly and easterly

phases of the QBO, a more rigorous analysis of the observations and detailed investigation of the basic dynamics is needed.

A deeper exploration of the ability of the modified *Held* (2000) scaling theory to reproduce the seasonality of the tropical belt width and edge latitudes is also warranted. It is remarkable that by simply parameterizing basic seasonal structures of the ITCZ latitude, tropopause height, and fractional dry stability, one can produce a seasonal cycle of Hadley cell and subtropical jet edge latitudes and widths broadly consistent with observations. Future research could, in the spirit of *Held and Hou* (1980) and *Lindzen and Hou* (1988), work with numerical integrations of the full non-equilibrium shallow water model on which the scaling theory is based. There is also the prospect of using an idealized aquaplanet general circulation model similar to that used by *Frierson et al.* (2006) to study the full dynamics of the Hadley cell. For example, the possible effects of stationary eddies and monsoonal circulations on the tropical belt edge latitudes could easily be explored by comparing the resulting circulations with and without topography. A full gamut of models, from equilibrium scaling arguments up to general circulation models, can be used to isolate the most important influences on the seasonality and interannual variability of the tropical belt edge latitudes.

Finally, the lag of the Hadley cell edge relative to the subtropical jet core and tropopause break demands to be explored in detail. Coming from the perspective of AM-conserving scaling theories, where the jet emerges from AM-conservation in the Hadley cell, the clear 1-month lag between the Hadley cell and the subtropical jet in the Northern Hemisphere is an indication that the jet is responding to some extratropical forcing faster than the overturning circulation. Given the hemispheric asymmetry, with no evidence of a

65

monthly-timescale lag in the Southern Hemisphere, it may be the enhanced eddy activity, the monsoonal circulation, or a combination of both in the Northern Hemisphere that is modulating the tropical belt edge latitude. Simulations with an aquaplanet model and a mutli-layer shallow water model could be used to study these hemispheric differences. These simulations will grant the ability to study these circulations on hourly rather than monthly timescales, permitting a more detailed characterization of the lag. It is imperative to characterize these different regimes if the dynamics of the seasonality, interannual variability, and ongoing decadal trends in the width of the tropical belt are to be better understood.

7 References

Andrews, D. G., J. Holton, and C. Leovy (1987), Middle Atmosphere Dynamics. Academic Press.

Anthes, R. A. et al. (2008), The COSMIC/Formosat-3 mission: Early results, *B. Am. Meterol. Soc.*, 89, 313-333.

Archer, C. L. and K. Caldeira (2008), Historical trends in the jet streams, *Geophys. Res. Lett.*, 35, L08803, doi:10.1029/2008GL033614.

Baldwin, M. P., et al. (2001), The quasi-biennial oscillation, *Rev. Geophys.*, 39(2), 179229, doi:10.1029/1999RG000073.

Bengtsson, L., Hodges, K. I., and Hagemann, S. (2004), Sensitivity of the ERA40 reanalysis to the observing system: determination of the global atmospheric circulation from reduced observations, *Tellus A*, 56: 456-471. doi: 10.1111/j.1600-0870.2004.00079.x.

Birner, T. (2010), Recent widening of the tropical belt from global tropopause statistics: Sensitivities, *J. Geophys. Res.*, 115, D23109, doi:10.1029/2010JD014664.

Birner, T. (2010), Residual Circulation and Tropopause Structure. *J. Atmos. Sci.*, 67, 25822600. doi: http://dx.doi.org/10.1175/2010JAS3287.1.

Bony, S. and J.-L. Dufresne (2005), Marine boundary layer clouds at the heart of tropical cloud feedback uncertainties in climate models, *Geophys. Res. Lett.*, 32, L20806, doi:10.1029/2005GL023851.

Bretherton, C. S., M. Widmann, V. P. Dymnikov, J. M. Wallace, and I. Blade (1999), The Effective Number of Spatial Degrees of Freedom of a Time-Varying Field, *J. Climate*, 12, 19902009. doi:http://dx.doi.org/10.1175/1520-0442(1999)012¡1990:TENOSD¿2.0.CO;2.

Ceppi, P., and D. Hartmann (2012): On the Speed of the Eddy-Driven Jet and the Width of the Hadley Cell in the Southern Hemisphere. *J. Climate*, doi:10.1175/JCLI-D-12-00414.1, in press.

Chen, G., and I. M. Held (2007), Phase speed spectra and the recent poleward shift of Southern Hemisphere surface westerlies, *Geophys. Res. Lett.*, 34, L21805, doi:10.1029/2007GL031200.

Davis, S. M. and K. H. Rosenlof (2012): A Multidiagnostic Intercomparison of Tropical-Width Time Series Using Reanalyses and Satellite Observations, *J. Climate*, 25, 10611078, doi: http://dx.doi.org/10.1175/JCLI-D-11-00127.1.

Lorenz, D. J. and E.T. DeWeaver (2007), Tropopause height and zonal wind response to global warming in the IPCC scenario integrations, *J. Geophys. Res.*, 112, D10119.

Dee, D. P. et al. (2011), The ERA-Interim reanalysis: configuration and performance of the data assimilation system, *Q.J.R. Meteorol. Soc.*, 137: 553597, doi:10.1002/qj.828.

Dima, I. M., J. M. Wallace, (2003), On the seasonality of the Hadley cell, *J. Atmos. Sci.*, 60, pp. 1522-1527.

Fischlin, A. et al. (2007), Ecosystems, their properties, goods, and services. Climate Change 2007: Impacts, Adaptation and Vulnerability. Contribution of Working Group II to the Fourth Assessment Report of the Intergovernmental Panel on Climate Change, M.L. Parry, O.F. Canziani, J.P. Palutikof, P.J. van der Linden and C.E. Hanson, Eds., Cambridge University Press, Cambridge, 211-272.

Fjeldbo, G. and V. R. Eshelman (1971): The neutral atmosphere of Venus as studied with the Mariner V radio occultation experiment, *Astron. J.*, 76, 123-140.

Frierson, D. M. W. (2006), Robust increases in midlatitude static stability in simulations of global warming, *Geophys. Res. Lett.*, 33, L24816, doi:10.1029/2006GL027504.

Frierson, D. M. W., J. Lu, and G. Chen (2007), Width of the Hadley cell in simple and comprehensive general circulation models, *Geophys. Res. Lett.*, 34, L18804, doi:10.1029/2007GL031115.

Frierson, D. M. W. and N. A. Davis (2011), The seasonal cycle of midlatitude static stability over land and ocean in global reanalyses, *Geophys. Res. Lett.*, 38, L13803, doi:10.1029/2011GL047747.

Frierson, D. M. W., I. M. Held, P. Zurita-Gotor (2006), A Gray-Radiation Aquaplanet Moist GCM. Part I: Static Stability and Eddy Scale, *J. Atmos. Sci.*, 63, 25482566. doi: http://dx.doi.org/10.1175/JAS3753.1.

Fu, Q. and P. Lin (2011), Poleward Shift of Subtropical Jets Inferred from Satellite-Observed Lower-Stratospheric Temperatures, *J. Climate*, 24, 55975603, doi:http://dx.doi.org/10.1175/JCLI-D-11-00027.1.

Held, I. M. and A. Y. Hou (1980), Nonlinear Axially Symmetric Circulations in a Nearly Inviscid Atmosphere, *J. Atmos. Sci.*, 37, 515533. doi:http://dx.doi.org/10.1175/1520-0469(1980)037¡0515:NASCIA¿2.0.CO;2.

Held, I.M. (2000), The general circulation of the atmosphere, paper presented at 2000 Woods Hole Oceanographic Institute Geophysical Fluid Dynamics Program, Woods Hole Oceanographic Institute, Woods Hole, Mass. http://gfd.whoi.edu/proceedings/2000/PDFvol2000.html

Hu, Y. and Q. Fu (2007), Observed poleward expansion of the Hadley circulation since 1979, *Atmos. Chem. Phys.*, 7, 5229-5236, doi:10.5194/acp-7-5229-2007.

Holton, J. R. (1994), *An Introduction to Dynamic Meteorology*, Academic Press, New York.

Hudson, R. D. (2012), Measurements of the movement of the jet streams at mid-latitudes, in the Northern and Southern Hemispheres, 1979 to 2010, *Atmos. Chem. Phys.*, 12, 7797-7808, doi:10.5194/acp-12-7797-2012.

Johanson, C. M. and Q. Fu (2009): Hadley Cell Widening: Model Simulations versus Observations, *J. Climate*, 22, 27132725. doi:http://dx.doi.org/10.1175/2008JCLI2620.1.

Kalnay, E., M. et al. (1996), The NCEP/NCAR 40-Year Reanalysis Project. *Bull. Amer. Meteor. Soc.*, 77, 437471.
doi:http://dx.doi.org/10.1175/1520-0477(1996)077¡0437:TNYRP¿2.0.CO;2.

Kang, S. M. and J. Lu (2012), Expansion of the Hadley cell under global warming: winter versus summer, *J. Climate*, doi:http://dx.doi.org/10.1175/JCLI-D-12-00323.1.

Kim, H. and S. Lee (2001), Hadley Cell Dynamics in a Primitive Equation Model. Part II: Nonaxisymmetric Flow, *J. Atmos. Sci.*, 58, 28592871, doi:
http://dx.doi.org/10.1175/1520-0469(2001)058¡2859:HCDIAP¿2.0.CO;2.

Kundzewicz, Z.W. et al. (2007): Freshwater resources and their management. Climate Change 2007: Impacts, Adaptation and Vulnerability. Contribution of Working Group II to the Fourth Assessment Report of the Intergovernmental Panel on Climate Change, M.L. Parry, O.F. Canziani, J.P. Palutikof, P.J. van der Linden and C.E. Hanson, Eds., Cambridge University Press, Cambridge, UK, 173-210.

Kursinski, E.R. et al. (1996), Initial Results of Radio Occultation Observations of Earth's Atmosphere Using the Global Positioning System, *Science*, Volume 271, Issue 5252, pp. 1107-1110, doi:10.1126/science.271.5252.1107.

Kursinski, E. R., G. A. Hajj, J. T. Schofield, R. P. Linfield and K. R. Hardy (1997), Observing the Earths atmosphere with radio occultation measurements using the Global Positioning System, *J. Geophys. Res.*, 102(D19), 23429-23465.

Kursinski, E. R., G. A. Hajj, S. S. Leroy, Herman, B. (2000), The GPS radio occultation technique, *Terrestrial, atmospheric, and oceanic sciences*, Vol. 11, No. 1, 53-114.

Lanzante, J. R. (2005), A Cautionary Note on the Use of Error Bars. *J. Climate*, 18, 36993703. doi:http://dx.doi.org/10.1175/JCLI3499.1

Leroy, S. S., C. O. Ao, O. Verkhoglyadova (2012), Mapping GPS Radio Occultation Data by Bayesian Interpolation, *J. Atmos. Oceanic Technol.*, 29, 10621074. doi:
http://dx.doi.org/10.1175/JTECH-D-11-00179.1

Lindzen, R. S. and A. V. Hou (1988), Hadley Circulations for Zonally Averaged Heating Centered off the Equator, *J. Atmos. Sci.*, 45, 24162427,
doi:http://dx.doi.org/10.1175/1520-0469(1988)045¡2416:HCFZAH¿2.0.CO;2.

Lu, J., G. Chen, D. M. W. Frierson (2008) Response of the Zonal Mean Atmospheric Circulation to El Nio versus Global Warming, *J. Climate*, 21, 58355851. doi:
http://dx.doi.org/10.1175/2008JCLI2200.1.

Lu, J., G. A. Vecchi, and T. Reichler (2007), Expansion of the Hadley cell under global warming, *Geophys. Res. Lett.*, 34, L06805, doi:10.1029/2006GL028443.

Maruyama, T. (1997), The quasi-biennial oscillation (QBO) and equatorial waves - a
historical review, *Meteo. and Geophys*, 48, 1-17.

Meehl, G. A. et al. in Climate Change 2007: The Physical Science Basis. Contribution of
Working Group I to the Fourth Assessment Report of the Intergovernmental Panel on
Climate Change (eds Solomon, S. et al.) (Cambridge University Press, Cambridge, UK,
2007).

Naujokat, B. (1986), An update of the observed quasi-biennial oscillation of the
stratospheric winds over the tropics, . *Atmos. Sci.*, 43, 1873-1877.

North, G. R., T. L. Bell, R. F. Cahalan, F. J. Moeng (1982), Sampling Errors in the
Estimation of Empirical Orthogonal Functions, *Mon. Wea. Rev.*, 110, 699706, doi:
http://dx.doi.org/10.1175/1520-0493(1982)110¡0699:SEITEO¿2.0.CO;2.

Pawson, S., K. Labitzke, R. Lenschow, B. Naujokat, B. Rajewski, M. Wiesner, and R.-C.
Wohlfahrt, (1993), Climatology of the Northern Hemisphere stratosphere derived from
Berlin analyses. Part 1: Monthly means, Meteorologische Abhandlungen, F.U. Berlin,
Serie A, Band 7.3, Verlag Dietrich Reimer, Berlin.

Plumb, R. A. (1977), The interaction of two internal waves with the mean flow:
Implications for the theory of the quasi-biennial oscillation, *J. Atmos. Sci.*, 34, 18471858.

Reid, G. C. and K. S. Gage (1981), On the Annual Variation in Height of the Tropical
Tropopause, *J. Atmos. Sci.*, 38, 19281938. doi:
http://dx.doi.org/10.1175/1520-0469(1981)038¡1928:OTAVIH¿2.0.CO;2.

Rienecker, M.M. et al. (2011), MERRA - NASA's Modern-Era Retrospective Analysis for
Research and Applications. *J. Climate*, 24, 3624-3648, doi:10.1175/JCLI-D-11-00015.1.

Santer, B. D., M. F. Wehner, T. M. L. Wigley, R. Sausen, G. A. Meehl, K. E. Taylor, and
W. Bruggemann (2003), Contributions of anthropogenic and natural forcing to recent
tropopause height changes, *Science*, 301(5632), 479-483.

Schneider, T. (2006), The general circulation of the atmosphere, *Annual Reviews of Earth
and Planetary Sciences*, 34, 655-688.

Scott, R. K., and P. H. Haynes (1998), Internal interannual variability of the extratropical
stratospheric circulation: The low latitude flywheel. *Q. J. R. Meteor. Soc.*, 124, 2149
2173.

Seidel, D. J., R. J. Ross, J. K. Angell, and G. C. Reid (2001), Climatological characteristics
of the tropical tropopause as revealed by radiosondes, *J. Geophys. Res.*, 106(D8),
78577878, doi:10.1029/2000JD900837.

Seidel, D.J., and W.J. Randel (2006): Variability and trends in the global tropopause
estimated from radiosonde data. *J. Geophys. Res.*, 111, D21101,
doi:10.1029/2006JD007363.

Seidel, D.J. and W.J. Randel (2007), Recent widening of the tropical belt: Evidence from tropopause observations, *J. Geophys. Res.*, 112, D20113, doi:10.1029/2007JD008861.

Seidel, D. J., Q. Fu, W. J. Randel and T. J. Reichler (2008), Widening of the tropical belt in a changing climate, *Nature Geoscience*, 1, 21 - 24, doi:10.1038/ngeo.2007.38.

Simpson, I. R., M. Blackburn, and J. D. Haigh (2009), The Role of Eddies in Driving the Tropospheric Response to Stratospheric Heating Perturbations, *J. Atmos. Sci.*, 66, 13471365, doi:http://dx.doi.org/10.1175/2008JAS2758.1.

Singh, M. S., P. A. OGorman (2012), Upward Shift of the Atmospheric General Circulation under Global Warming: Theory and Simulations, *J. Climate*, 25, 82598276. doi: http://dx.doi.org/10.1175/JCLI-D-11-00699.1.

Stachnik, J. P. and C. Schumacher (2011), A comparison of the Hadley circulation in modern reanalyses, *J. Geophys. Res.*, 116, D22102, doi:10.1029/2011JD016677.

Strong C. and R.E. Davis (2006), Temperature-related trends in the vertical position of the summer upper tropospheric surface of maximum wind, *International Journal of Climatology*, 26, 1977-1997, doi:10.1002/joc1344.

Son, S.-W., N.F. Tandon, and L.M. Polvani (2011), The fine-scale structure of the global tropopause derived from COSMIC GPS radio occultation measurements, *J. Geophys. Res.*, 166, D20113, doi:10.1029/2011JD016030.

Trenberth, K.E. (1997), The Definition of El Nino, *Bulletin of the American Meteorological Society*, 78, 2771-2777.

Trenberth, K. E., D. P. Stepaniak, J. W. Hurrell, and M. Fiorino (2001), Quality of Reanalyses in the Tropics, *J. Climate*, 14, 14991510, doi:http://dx.doi.org/10.1175/1520-0442(2001)014¡1499:QORITT¿2.0.CO;2.

Waliser, D. E., and C. Gautier (1993), A Satellite-derived Climatology of the ITCZ, *J. Climate*, 6, 21622174. doi: http://dx.doi.org/10.1175/1520-0442(1993)006¡2162:ASDCOT¿2.0.CO;2.

Waliser, D. E., Z. Shi, J. R. Lanzante, and A. H. Oort (1999), The Hadley circulation: assessing NCEP/NCAR reanalysis and sparse in-situ estimates, *Climate Dynamics*, 15(10), 719-735.

Walker, C. C., and T. Schneider (2006), Eddy influences on Hadley circulations: Simulations with an idealized GCM. *J. of Atmos. Sci.*, 63, 3333-3350.

Wickert, J., et al. (2001), Atmosphere sounding by GPS radio occultation: First results from CHAMP, *Geophys. Res. Lett.*, 28(17), 32633266, doi:10.1029/2001GL013117.

World Meteorological Organization (1957), Meteorology - A three-dimensional science, *WMO 25 Bull.*, 6, (Oct), 134138, 1957.